

Numerical simulation of a prostate tumor growth model by the RBF-FD scheme and a semi-implicit time discretization

Vahid Mohammadi^a, Mehdi Dehghan^{a,*}, Stefano De Marchi^b

^a*Department of Applied Mathematics, Faculty of Mathematics and Computer Sciences, Amirkabir University of Technology, No. 424, Hafez Ave., 15914, Tehran, Iran*

^b*Department of Mathematics "Tullio Levi-Civita", University of Padua, Italy*

Abstract

The aim of this work consists of finding a suitable numerical method for the solution of the mathematical model describing the prostate tumor growth, formulated as a system of time-dependent partial differential equations (PDEs), which plays a key role in the field of mathematical oncology. In the literature on the subject, there are a few numerical methods for solving the proposed mathematical model. The localized prostate cancer growth is known as a moving interface problem, which must be solved in a suitable stable way. The mathematical model considered in this paper, is a system of time-dependent nonlinear PDEs that describes the interaction between cancer cells, nutrients and prostate specific antigen (PSA). Here, we first derive a non-dimensional form of the studied mathematical model using the well-known non-dimensionalization technique, which it makes easier to implement different numerical techniques. Afterward, the analysis of the numerical method describing the two-dimensional prostate tumor growth problem, based on radial basis function-generated finite difference (RBF-FD) scheme, in combination with a first-order time discretization has been done. The numerical technique we use, does not need the use of any adaptivity techniques to capture the features in the interface. The discretization leads to solving a linear system of algebraic equations solved via the biconjugate gradient stabilized (BiCGSTAB) with zero-fill incomplete lower-upper (ILU) preconditioner. Comparing the results obtained in this investigation with those reported in the recent literature, the proposed approach confirms the ability of the developed numerical scheme. Besides, the effect of choosing constant parameters in the mathematical model is verified by many simulations on rectangular and circular domains.

Keywords: Time-dependent nonlinear partial differential equations, radial basis function-generated finite difference scheme, non-dimensionalization technique, biconjugate gradient stabilized gradient, mathematical oncology, prostate tumor growth, moving interface problem.

2010 MSC: 92C17, 35Q35, 35Q92.

*Corresponding author

Email addresses: v.mohammadi@aut.ac.ir, v.mohammadi.aut@gmail.com (Vahid Mohammadi), mdehghan@aut.ac.ir, mdehghan.aut@gmail.com (Mehdi Dehghan), demarchi@math.unipd.it (Stefano De Marchi)

1. Introduction

Cancer is the result of abnormal proliferation of any of the different kinds of cells in the body. Accordingly, there are a hundred distinct types of cancer, which are different in responding to treatments and in behaviors [10]. Aging men may face to genitourinary diseases called *Prostate Cancer* (PCa) or the *Benign Prostatic Hyperplasia* (BPH) [52]. PCa is known as an adenocarcinoma (approximately 95 percentage), which means a type of cancer (originated in an epithelial tissue) that starts in the glands that lines the inside of one of the organs. Facts and figures given in [52] show that the second most common cancer and the fifth leading cause of death from cancer in men worldwide is PCa. Generally, the development process of PCa is as follows. At the first stage, it grows locally within the prostate. After that, the tumor tends to invade the surrounding tissues. Finally, it migrates to distant tissues by leaving some malignant cells from the original tumor and getting into the bloodstream (metastasis) [3, 4, 23, 36, 51].

As mentioned in [50], there are two main reasons for studying PCa in tissue-scale:

1. the prostate is a small organ;
2. the tumor growth can be estimated by measuring a PCa biomarker in blood, called *serum Prostate-Specific Antigen (PSA)*, and it may enable in vivo model validation [50].

To predict clinical outcomes and design the optimal therapies on a patient, constructing and developing mathematical models with the simulations of diseases and their treatments, can be useful [50]. The tumor growth is followed by a complex biological mechanisms, which occurs at different scales, i.e., the molecular, cellular, and tissue scales [83]. In recent years, there are different types of mathematical models, which are able to describe the process of the tumor growth in tissue scale at two main stages: *avascular* and *vascular* (see among the many ones: [2, 4, 16, 17, 23, 36, 49, 58]). In some studies the role of nutrients is also considered in the mathematical model of the process of the tumor growth (for instance in [34, 35, 40, 46, 79, 80]). In fact, healthy and tumoral cells have a competition to gain nutrients, proliferate and control cell density in the harsh tumoral environment. To formulate a mathematical model describing PCa, in [50] the authors have derived a new phenomenological model based on a system of time-dependent nonlinear PDEs. Besides, they have assumed that the growth of PCa depends only on a nutrient, which is mainly composed of glucose [50]. More recently, in [52], a new mathematical model in tissue-scale has been derived, which shows the mechanical interaction of PCa and BPH. As a completion, the model describing PCa under the effect of therapies (i.e., chemotherapy and antiangiogenic therapy) has been presented in [9].

Since the exact solution of the model describing PCa is not available, numerical methods play an important role in simulating the process. There exist few numerical methods to find the approximate solution of the mathematical model of PCa. For example, the method based on hierarchically refined and coarsened splines is applied for space discretization and generalized- α method for time discretization in [51]. An isogeometric discretization based on the Galerkin method has been employed to discretize the space variables of the PCa model under the effect of therapies, while the generalized- α method is used to discretize the time variable (cf. [9]).

So far, meshless methods were not applied to find the numerical solution for the mathematical model of PCa [50]. These methods distinguish them from mesh-dependent methods, such as finite element

method (FEM) and finite volume method (FVM), for the following properties. Meshless methods do not need to generate the underlying mesh (or triangulation) for approximation [24, 59, 78]. With this, they can be easily implemented for finding the numerical solution of high-dimensional PDEs with arbitrary domain geometry. Overall, these techniques are categorized into strong form, weak form and local weak form, which are derived by choosing a suitable space of test functionals. Besides, the trial space would be constructed using an approximation based on scattered data. Method based on *Radial Basis Functions (RBFs)* and *Moving Least Squares (MLS) approximation* are two well-known meshless techniques [24, 59, 78]. The methods based on RBF approximation are known as powerful numerical approaches for solving problems in high-dimensional spaces [24, 78]. Recently, new techniques based on RBFs, namely rational RBFs partition of unity (RBFs-PU), RBFs-PU based on variably scaled kernels (VSKs) and RBFs combined with variably scaled discontinuous kernels (VSDKs) have been developed in [20, 21, 22]. Also, some applications of VSKs method for solving the time-dependent PDEs can be found in [14, 61]. See also [47, 53, 54, 60, 76].

In 1990, Ed Kansa [44] applied the traditional RBF method for finding a new numerical solution of an elliptical PDE. His technique, based on collocation, gave rise to a linear (nonlinear) system with a full ill-conditioned matrix [24, 78]. In 2000 Tolstykh introduced the initial idea of the RBF-FD scheme [75]. This approach can also be viewed as the local radial basis function-differential quadrature (LRBF-DQ) scheme (cf. e.g. [72]) presented in a more general way in [81]. The scheme is known also as a *generalization of the classical finite difference (FD) method because of the fact that* instead of using polynomial test functions, d dimensional RBFs are used (cf. [31, 45, 64]). Hence, the RBF-FD method, is more flexible since it works on different geometries with unstructured node layouts (cf. [31, 45]). It also benefits of the possibility of augmenting the stencil with polynomial terms, by adding constraints associated with the RBF expansion coefficients [6]. By using polyharmonic splines (PHS) kernels, it is argued (analytically and numerically) that using the RBF interpolant augmented with polynomials overcomes the stagnation errors, and the order of convergence of the method depends only on the highest augmented polynomial degree (cf. [6] and see also the last paragraph in Section 4). On the other hand, to improve the accuracy and rate of convergence of the RBF-FD scheme, it is possible to use more nodes in each stencil (called also *support domain* or *local sub-domain* or *local domain of influence*) without the need of approximating the derivatives, as pointed out in [6, 32]. Moreover, applying this method for discretizing the differential operator of a PDE, gives rise to a sparse matrix and this matrix has smaller condition number than that originated with traditional global RBF approaches [31, 32, 33]. We recall the role of the choice of the *shape parameter* in the stability and convergence of RBF approximation (see Sections 4 and 7). Interested readers can refer to [6, 7, 19, 26, 27, 31, 32, 33, 67, 69, 70] and references therein.

As recent results on the RBF-FD approach, in [69] the authors introduced a generalization of the RBF-FD, called the *overlapped RBF-FD scheme*. This approach involves an overlap parameter, say δ , which recovers the standard RBF-FD scheme when $\delta = 1$. In [6], the RBF interpolation augmented with polynomials (RBF+poly) has been presented as a constrained optimization problem, and has derived the convergence analysis for the local RBF augmented with polynomials (LRBF+poly). Also, the LRBF+poly method with PHS kernel has been rewritten as a *best* least squares approximation and quadratic minimization problem, deriving the convergence order of the method [7]. Recently, author of [56] have introduced a new local RBF scheme, namely the *direct RBF partition of unity (D-RBF-PU)*

which is a new RBF-FD scheme in a PU setting. It also is shown that the method is much faster and, in some situations more accurate, than the original form of the RBF-FD.

Over the past two decades, the RBF-FD technique has been successfully applied to solve numerically practical mathematical models defined in high-dimensional spaces. For example, it has been applied to solve shallow water equations on the sphere [26], reaction-diffusion equations [67], reaction-diffusion equations on surfaces [68], Navier-Stokes equations [27], high-dimensional nonlinear Schrödinger equations [15], some PDEs on surfaces [71], the damped Kuramoto-Sivashinsky (KS) equation [18] and Shan-Chen model [1].

The main contributions to the numerical solution of the model are here summarized as follows:

- The derivation of a non-dimensional form of the mathematical model, introduced in [50], allowing an easier implementation of different numerical methods.
- The use of the RBF-FD scheme for discretizing the space variables.

In comparison with known numerical methods, such those in [50, 51], the new technique has the following advantages.

- The implementation of the RBF-FD technique is simpler than the methods in [50, 51].
- Using the RBF-FD technique, we do not need any specific background mesh or triangulation and any adaptivity algorithms.
- The results are on rectangles and on circular domains, but can be extended to other geometries in two-dimensions without any further new implementation.

We have then applied a semi-implicit backward differential formula of first-order (SBDF1) to discretize the time variable. This gives a new fully discrete scheme that is a linear system at any time step, in which the coefficient matrix is large and sparse. To solve it efficiently, we adopt known techniques, such those described in [17, 47, 58, 60]. In particular, we use the BiCGSTAB method with zero-fill ILU preconditioner. As a note, it is possible to use other time discretizations, such as explicit (conditionally stable) method, implicit-explicit and implicit schemes, for example see [70].

The outline of this manuscript is as follows. In Section 2, we briefly review the mathematical model, which will be solved numerically by a meshless technique in space and with the SBDF1 in time. In Section 3, a non-dimensional form of the model is derived. The details of the applied meshless technique are provided in Section 4. The fully discrete scheme is given in Section 6. In Section 7, some simulation results, based on parameters given in [51] and also parameters based on clinical data provided in [50], are presented. Finally, in Section 8 we present some concluding remark.

2. The mathematical model

In this section, the mathematical model of the prostate tumor growth [50, 51] is briefly described. The interested reader may refer to [50, 51] to find out how the mathematical model is formulated, based on some required biological facts.

The PCa growth depends on nutrients, hormones and proteins. In this model, only cancerous and non-cancerous cells are considered. For describing the dynamics of glucose, a generic nutrient σ is considered. Furthermore, the model studied here describes the value of PSA (produced by the healthy and tumoral cells) observed by a blood testing (see [50, 51] for more details). Due to these explanations, a differential equation, which describes the dynamics of the tissue PSA is formulated: its variable is denoted by p . More specifically, all unknown space- and time-dependent variables of the mathematical model here considered, are defined as follows:

- $\varphi(\mathbf{x}, t)$: the concentration of the cell microstructure,
- $\sigma(\mathbf{x}, t)$: the concentration of the nutrient,
- $p(\mathbf{x}, t)$: the concentration of PSA,

where $\mathbf{x} \in \Omega \subset \mathbb{R}^d$ (here is $d = 2$), $t \in [0, T]$ and T is the final time.

The model we are considering has been already studied in [50, 51], consists of a set of three time-dependent PDEs. The first equation, showing the dynamic of the concentration of the cell microstructure, is

$$\frac{\partial \varphi}{\partial t} = \lambda \Delta \varphi - \frac{1}{\tau} F'(\varphi) + \chi \sigma - A \varphi, \quad (2.1)$$

where $\varphi =: \varphi(\mathbf{x}, t)$ is a phase field variable or an order parameter aimed to identify one phase from the other of tumor evolution. It also shows transitions from the value 0 (the healthy host tissue) to 1 (tumor region) ($t \in (0, T]$). Besides, $\varphi = 0.5$ indicates the interface implicitly. This equation is derived based on the phase field method (cf. [9, 37]). For instance, $F(\varphi) := 16\varphi^2(1 - \varphi)^2$ is a double-well potential.

In (2.1), the third term $\chi \sigma$, shows the growth due to nutrient. Indeed, the model assumes that tumor cells grow linearly in the presence of the nutrient at a rate χ . The fourth term, $-A \varphi$ represents apoptosis (programmed cell death). Following again [50, 51, 52], the tumor volume can be computed as

$$V_\varphi(t) := \int_{\Omega} \varphi \, d\mathbf{x}, \quad t \geq 0. \quad (2.2)$$

The second equation, shows the dynamic of the nutrient

$$\frac{\partial \sigma}{\partial t} = \epsilon \Delta \sigma + s - \delta \varphi - \gamma \sigma, \quad (2.3)$$

where $\sigma =: \sigma(\mathbf{x}, t)$, s indicates a constant nutrient supply, δ is the rate of consumption the nutrient by the tumor cells, and γ is the rate of natural decay. As a note, in (2.3), due to the results given in [8], here the effect of convection on the nutrient transport is negligible.

The last equation models the dynamic of PSA

$$\frac{\partial p}{\partial t} = \eta \Delta p + \alpha_h(1 - \varphi) + \alpha_c \varphi - \gamma_p p, \quad (2.4)$$

in which $p =: p(\mathbf{x}, t)$, α_h and α_c represent the rates of production of PSA using healthy and tumoral tissues per unit volume, respectively. The parameter γ_p is the rate of natural decay PSA that is followed by the first order kinetics. To obtain the value of serum PSA, we use the formula

$$P_s(t) = \int_{\Omega} p \, d\mathbf{x}, \quad t \geq 0. \quad (2.5)$$

Initial and boundary conditions must be considered for three unknowns, i.e., φ , σ and p . In this paper, we use zero-valued Dirichlet boundary conditions for all variables.

3. The non-dimensional form

In [51], equations (2.1)-(2.4) are solved numerically via a method consisting of a hierarchically refined and coarsened splines, without considering any non-dimensional approach. Here instead, we present a non-dimensional form of equations (2.1)-(2.4). To do so, we define the new dimensionless variables

$$\tilde{\sigma} = \frac{\sigma}{\sigma^*}, \quad \tilde{p} = \frac{p}{p^*}, \quad \tilde{t} = \frac{t}{t^*}, \quad \tilde{\mathbf{x}} = \frac{\mathbf{x}}{\mathbf{x}^*}, \quad (3.1)$$

with $\sigma^* = g/L$ and $p^* = g/L^2$ are the units of variables σ and p , respectively, where g and L represent *gram* and *litre*, respectively. The unit of time t^* corresponds to one year, and the characteristic length scale $\mathbf{x}^* := 0.1\text{cm}$ (cf. [36, 23]). Following [36], the value \mathbf{x}^* corresponds to the maximum invasion distance at the early stage of tumor. Its value, as firstly studied in [4], should be reasonably taken in the range $[0.1, 1]$ centimeters. Also, all constant parameters introduced in (2.1)-(2.4) should be written with their units such that the left-hand side and right-hand side of each equation have the same unit. Then, these constant parameters are divided by their units, which give dimensionless parameters (cf. [4, 23, 36]).

Hence, replacing (3.1) into (2.1)-(2.4) we get a non-dimensional form of the model,

$$\begin{aligned} \frac{\partial \varphi}{\partial \tilde{t}} &= \tilde{\lambda} \Delta \varphi - \frac{1}{\tilde{\tau}} F'(\varphi) + \tilde{\chi} \tilde{\sigma} - \tilde{A} \varphi, \\ \frac{\partial \tilde{\sigma}}{\partial \tilde{t}} &= \tilde{\epsilon} \Delta \tilde{\sigma} + \tilde{s} - \tilde{\delta} \varphi - \tilde{\gamma} \tilde{\sigma}, \\ \frac{\partial \tilde{p}}{\partial \tilde{t}} &= \tilde{\eta} \Delta \tilde{p} + \tilde{\alpha}_h (1 - \varphi) + \tilde{\alpha}_c \varphi - \tilde{\gamma}_p \tilde{p}, \end{aligned} \quad (3.2)$$

in which the quantities indicated with the tilde are now dimensionless. We do not use this notation for φ because it is already dimensionless. Hence, (3.2) is a type of reaction-diffusion system or a quasi-linear parabolic system. It is worth mentioning that, if $0 \leq \varphi(\mathbf{x}, 0) \leq 1$ a.e. for $\mathbf{x} \in \Omega$ then the solution of the above system uniquely exists with $0 \leq \varphi(\mathbf{x}, t) \leq 1$ a.e. $(\mathbf{x}, t) \in \Omega \times [0, T]$, as proved in [9, Theorem 3.1].

Remark. There are different reaction-diffusion systems in the literature such as Turing-type models, namely Gierer-Meinhardt [38], Gray-Scott [39], Lengyel-Epstein [48], Brusselator [42, 57], Selkov [65] and Schnakenberg [66]. But, the studied mathematical model here is different from those models due to the nonlinear term F' .

The boundary conditions for the unknowns φ , $\tilde{\sigma}$ and \tilde{p} are taken as follows:

$$\varphi(\mathbf{x}, t) = 0, \quad \tilde{\sigma}(\mathbf{x}, t) = 0, \quad \tilde{p}(\mathbf{x}, t) = 0, \quad \mathbf{x} \in \Omega, \quad t \geq 0. \quad (3.3)$$

As an example, in Table 1 we report the list of parameters used in [51], with the corresponding units and their non-dimensional counterparts.

Parameter	Value	Unit	Dimensionless parameter	Value
λ	1.6×10^5	$\mu m^2/year$	$\tilde{\lambda}$	0.16
τ	0.01	years	$\tilde{\tau}$	0.01
χ	600	$L/(g \cdot year)$	$\tilde{\chi}$	600
A	600	1/year	\tilde{A}	600
ϵ	5×10^6	$\mu m^2/year$	$\tilde{\epsilon}$	5
s	2.7	$g/(L \cdot day)$	\tilde{s}	9.8550×10^2
δ	2.75	$g/(L \cdot day)$	$\tilde{\delta}$	1.0038×10^3
γ	1000	1/year	$\tilde{\gamma}$	1000
η	1.6×10^5	$\mu m^2/year$	$\tilde{\eta}$	0.16
α_h	6.25	$(ng/mL)/(cm^3 \cdot year)$	$\tilde{\alpha}_h$	0.00625
α_c	$15\alpha_h$	$(ng/mL)/(cm^3 \cdot year)$	$\tilde{\alpha}_c$	$15\tilde{\alpha}_h$
γ_p	100	1/year	$\tilde{\gamma}_p$	100

Table 1: Example of the used constant parameters in the proposed mathematical model [51] with their non-dimensionalized counterparts.

In the next section, we introduce the numerical method which will be applied to approximate the unknowns φ , $\tilde{\sigma}$ and \tilde{p} in (3.2), together with the boundary conditions (3.3) for the space variables.

4. The RBF-FD technique

This section is devoted to briefly present the RBF-FD scheme that we are then applying as our discretization method. As was mentioned earlier, this technique is known also as an example of a *generalized FD scheme* [31, 45, 64]. Unlike to the standard FD scheme this method is based on Radial Basis Functions (RBF) approximation of the differential operators involved.

Just to recall, RBF approximation of functions is a linear combination of functions $\{\phi(\|\cdot - \mathbf{x}_j\|_2), j = 1, \dots, N\}$, where \mathbf{x}_j are (scattered) points, called centers, belonging to some domain $\Omega \subset \mathbb{R}^d$. The radial function $\phi : [0, \infty) \rightarrow \mathbb{R}$ can be considered *positive definite* or *conditionally positive definite* (cf. e.g. [24, 78])

Definition 4.1. [24, 78] *A continuous radial function ϕ is conditionally positive definite of order m on \mathbb{R}^d if*

$$\sum_{i=1}^N \sum_{j=1}^N c_i c_j \phi(\|\mathbf{x}_i - \mathbf{x}_j\|_2) > 0,$$

for any N pairwise distinct points $\mathbf{x}_1, \mathbf{x}_2, \dots, \mathbf{x}_N \in \mathbb{R}^d$ and any non zero vector $\mathbf{c} = [c_1, c_2, \dots, c_N]^T \in \mathbb{R}^N$ satisfying the following condition

$$\sum_{j=1}^N c_j p(\mathbf{x}_j) = 0, \quad \text{for all } p \in \mathbb{P}_{m-1}^d,$$

where \mathbb{P}_{m-1}^d is the space of d -variate polynomials of degree at most $m-1$. Also, ϕ is called positive definite if it is conditionally positive definite of order $m = 0$.

Examples of radial functions ϕ are provided in Table 2. The parameter ε is called *shape parameter* that affects the accuracy and stability of the RBF approximation, i.e., the so called *trade-off principle* that can be described as follows (cf. i.e. [24, 78]).

For a fixed shape parameter ε , increasing the number of nodes the error decreases, improving the accuracy, but on the other hand the interpolation matrix becomes more ill-conditioned. The trade-off principle suggests to find a suitable ε , say ε^* that balances the error versus the ill-conditioning of the approximation matrix. Below, in the Section 7, we briefly show this issue with some numerical results.

Besides, over the past two decades, some strategies have been introduced to overcome the ill-conditioning of the RBF approximation at small values of the shape parameter ε . Just to mention, the *contour-Padé* method was studied for multiquadrics by Fornberg and Wright [28]. The *RBF-QR* on the sphere [29] is one of the first attempts to avoid the ill-conditioning when $\varepsilon \rightarrow 0$: the so called flat-limit case. So far, this algorithm has been extended to $d \geq 1$ dimensional spaces, only for the *Gaussians* [25, 30], and also has been applied in the context of RBF-FD scheme [45]. Furthermore [32] has introduced the *RBF-GA algorithm* to bypass the ill-conditioning of the RBF-FD method, when the Gaussians are computed at small shape parameters, to obtain the stencil weights. Recently, the *RBF-RA method* has been introduced, which is based on a new method for rational approximation (RA) of vector-valued analytic functions. It turns out to be more accurate, robust, and easier to implement with respect to the *contour Padé approximation* [82]. Here, we do not discuss this issue of the ill-conditioning at small values of ε while referring the interested readers to the quoted references for details.

RBF	$\phi(r)$	Parameters	Order m
Gaussian (GA)	$\exp(-\varepsilon^2 r^2)$	$\varepsilon > 0$	0
Inverse multiquadric(IMQ)	$(1 + \varepsilon^2 r^2)^{-\beta}$	$\beta > d/2, \varepsilon > 0$	0
Multiquadric (MQ)	$(1 + \varepsilon^2 r^2)^\beta$	$\beta > 0, \beta \notin \mathbb{N}, \varepsilon > 0$	$\lceil \beta \rceil$
Wendland's functions	$\phi_{d,k}(\varepsilon r)$	$k \in \mathbb{N}_0, d \in \mathbb{N}, \varepsilon > 0$	0

Table 2: Some examples of RBF with $r := \|\mathbf{x}\|_2, \mathbf{x} \in \mathbb{R}^d$ [24, 78].

According to the third row of Table 2, choosing $0 < \beta < 1$ gives an RBF which is conditionally positive definite of order one [24, 78], but due to [78, Theorem 8.5] or [24, Theorem 9.7], there is no need to add the constant term to the interpolation problem, and thus the matrix $A_{\phi,X} := [\phi(\|\mathbf{x}_i - \mathbf{x}_j\|_2)]_{1 \leq i,j \leq N}$ is invertible. To find out more details about RBF approximation and its error analysis, we refer to [24, 78]

and all references related to this subject. For the definition and construction of the Wendland's functions $\phi_{d,k}(\varepsilon r)$ in the last row of Table 2, refer to [78, Chapter 9].

We now present the details of the RBF-FD technique. To do so, suppose that N scattered points (nodes) $X = \{\mathbf{x}_1, \dots, \mathbf{x}_N\} \subset \Omega \subset \mathbb{R}^d$ are chosen. The idea is finding an RBF approximation of $\Delta u(\mathbf{x})$ at the point \mathbf{x}_1 , with $u : \Omega \rightarrow \mathbb{R}$ the unknown function, solution of a differential problem. We then suppose that $n \ll N$ nodes, i.e., $P_1 = \{\mathbf{x}_j\}_{j=1}^n$ are in a neighborhood of our point, i.e., $\mathbf{x}_1 \in X$ located at the center of P_1 (it also called the stencil). At the first, we define the family of indices

$$I(\mathbf{x}_1) = \{j \in \{1, 2, \dots, N\} \mid \|\mathbf{x}_j - \mathbf{x}_1\|_2 \leq \delta\}, \quad (4.1)$$

where δ is the radius of influence. Thus, $|I(\mathbf{x}_1)| = n$ (see Figure 1 which shows a domain of influence of an interior point), and $\Delta u(\mathbf{x}_1)$ can be approximated by (cf. e.g. [5, 18, 26, 27, 32, 33, 81])

$$\Delta u(\mathbf{x}_1) \approx \sum_{j=1}^n w_{1j}^L u_j = (\mathbf{w}^L)^T \mathbf{u}|_{P_1}, \quad (4.2)$$

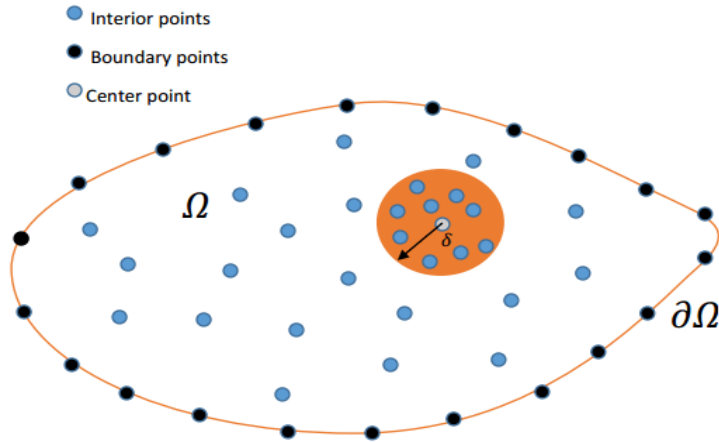


Figure 1: In orange a small circle representing the local domain of influence of a point inside Ω with $\partial\Omega$ its boundary (this picture is taken from [18]).

where $\mathbf{w}^L = [w_{11}, w_{12}, \dots, w_{1n}]^T$ is the stencil weights vector, and $\mathbf{u}|_{P_1}$ is the vector of nodal values at P_1 . To compute the weights vector \mathbf{w}^L , it requires the stencil to reproduce all functions spanned by the translates $\{\phi(\|\cdot - \mathbf{x}_j\|_2) : \mathbf{x}_j \in P_1\}$ (cf. [45]). Therefore, we have

$$\sum_{j=1}^n w_{1j}^L \phi(\|\mathbf{x}_i - \mathbf{x}_j\|_2) = \Delta \phi(\|\mathbf{x}_i - \mathbf{x}_1\|_2), \quad i = 1, 2, \dots, n. \quad (4.3)$$

The matrix form of relation (4.3) can be written as follows

$$A_{\phi, P_1} \mathbf{w}^L = \mathbf{b}, \quad (4.4)$$

where

$$A_{\phi, P_1} = [\phi(\|\mathbf{x}_i - \mathbf{x}_j\|_2)]_{1 \leq i, j \leq n}, \quad \mathbf{w}^L = [w_{1j}^L]_{1 \leq j \leq n}^T, \quad \mathbf{b} = [\Delta\phi(\|\mathbf{x}_i - \mathbf{x}_1\|_2)]_{1 \leq j \leq n}^T.$$

Then, we repeat the procedure for the other nodes, $\mathbf{x}_2, \dots, \mathbf{x}_N$.

Finally, a sparse differentiation matrix, say W_X^L , with size $N \times N$ can be constructed, by re-arranging the computed weights for each node.

Here, we should also mention that, when PHS kernels are considered (which are independent of ε), the weights can be obtained by employing *scalable* stencils (see e.g. [13, Section 5], [43, Subsection 6.1]). These kernels are obtained from the univariate functions

$$\phi_{m,d}(r) = \begin{cases} r^{2m-d} \log(r), & 2m - d \text{ even} \\ r^{2m-d}, & 2m - d \text{ odd} \end{cases} \quad (4.5)$$

which are used by adding polynomials (*PHS+poly*) of orders $\ell \geq \lfloor m - d/2 \rfloor + 1$ so that we can approximate the pointwise derivatives of order s in the *Sobolev spaces* $W_2^m(\mathbb{R}^d)$ by function values at the stencil, with an *optimal convergence rates* $m - s - d/2$, s being the *scaling order* (or *homogeneity order*) (cf. [13]). This order is related to that of the linear functional defined on the *scalable spaces*, which are Beppo-Levi spaces (cf. [78, Chapter 10]). Here, we employ a multiquadric (MQ) as radial basis function (see Eq. (7.1)) with *nonscalable* stencils and fixed shape parameter ε for obtaining the stencil weights. Of course, **one gets ill-conditioning of the local** interpolation matrices for small values of ε and/or small h (the largest distance between two nodes as the stencil size). To bypass this issue, it is possible to use some strategies such as the RBF-QR, the RBF-GA and the RBF-RA algorithms in the framework of RBF-FD scheme, as mentioned at the beginning of this section. As a note, in our implementations below, for solving Eq. (4.4) in each stencil we have applied the *backslash* command of MATLAB.

Concerning the convergence analysis of the nodal meshless methods, R. Schaback in [64, Theorem 1] provided a general form of classical elements of the convergence analysis for which the right-hand side of the relative error bound contains the product of the *stability* constant, the *consistency* bound and a *computational accuracy* (related to the linear algebra solver). The stability constant, that can be explicitly calculated for standard norms, can be numerically handled providing accurate estimates of it, as detailed in [64, §7].

Later on, D. Mirzaei [55] used the same approach to prove the error analysis of the Generalized Moving Least Squares (GMLS) approximation for solving a PDE problem on the sphere. O. Davydov in [11, 12] introduced error bounds for kernel-based numerical differentiation using the idea of *growth functions*, while V. Shankar [69] used Davydov's approach to prove local estimate of the augmented RBF-FD method. Recently, in [43] the authors have applied Schaback's theory with Davydov's extension to obtain the error bound of the weak-form for the RBF-FD method on each local stencil. In addition, V. Bayona [7] presented an error analysis based on local polynomial reproduction property, as it was used in the context of the MLS approximation, with *PHS* kernel applied in *LRBF+poly* method, with high degree

polynomials. In the paper he showed that the order of convergence of the RBF-FD method is $\mathcal{O}(h^{l+1})$ for the interpolation problem, where h is the average internodal distance within the stencil and l represents the degree of the polynomial in a d -dimensional space. Besides, he claimed that the size of stencil has insignificant effect on the accuracy of this method in computing the derivatives of a given function. The reader should also be aware that the unique stencil obtained by PHS kernels (4.5) by adding polynomials with order $\ell \geq \lfloor m - d/2 \rfloor + 1$ **has a convergence rate not better** than $m - s - d/2$ in the Beppo-Levi space (cf. [13, Corollary 5.2]). For more details on this subject, the interested reader is referred to the above references.

5. The semi-discrete problem

For this step we use the *Method of Lines (MOL)*. That is, first we derive the semi-discrete problem, by employing the RBF-FD technique for discretizing the spatial variables (3.2) with the boundary conditions (3.3), then, we apply a semi-implicit time-stepping scheme to solve the resulting system of ordinary differential equations (ODEs).

To this aim, let us consider a set of scattered nodes

$$X = \{\mathbf{x}_1, \mathbf{x}_2, \dots, \mathbf{x}_N\} = \{\mathbf{x}_1, \mathbf{x}_2, \dots, \mathbf{x}_{N_I}\} \cup \{\mathbf{x}_{N_I+1}, \mathbf{x}_{N_I+2}, \dots, \mathbf{x}_{N_I+N_B}\}$$

as trial points distributed in $\Omega \subset \mathbb{R}^2$, where $N := N_I + N_B$, N_I and N_B stand the number of interior and boundary nodes, respectively. The approximate solutions $\varphi(\mathbf{x}, t)$, $\tilde{\sigma}(\mathbf{x}, t)$ and $\tilde{p}(\mathbf{x}, t)$ at any $\mathbf{x} \in \Omega$ and $t \geq 0$, can then be written by using trial functions $w_j(\mathbf{x})$, $j \in I(\mathbf{x})$ as follows

$$\begin{aligned} \varphi(\mathbf{x}, t) &\approx \sum_{j \in I(\mathbf{x})} w_j(\mathbf{x}) \varphi_j(t), \\ \tilde{\sigma}(\mathbf{x}, t) &\approx \sum_{j \in I(\mathbf{x})} w_j(\mathbf{x}) \tilde{\sigma}_j(t), \\ \tilde{p}(\mathbf{x}, t) &\approx \sum_{j \in I(\mathbf{x})} w_j(\mathbf{x}) \tilde{p}_j(t). \end{aligned} \tag{5.1}$$

By using (5.1), we have

$$\begin{aligned} \Delta \varphi(\mathbf{x}, t) &\approx \sum_{j \in I(\mathbf{x})} \Delta w_j(\mathbf{x}) \varphi_j(t), \\ \Delta \tilde{\sigma}(\mathbf{x}, t) &\approx \sum_{j \in I(\mathbf{x})} \Delta w_j(\mathbf{x}) \tilde{\sigma}_j(t), \\ \Delta \tilde{p}(\mathbf{x}, t) &\approx \sum_{j \in I(\mathbf{x})} \Delta w_j(\mathbf{x}) \tilde{p}_j(t), \end{aligned} \tag{5.2}$$

where $\Delta w_j(\mathbf{x}) := w_j^L(\mathbf{x})$.

Replacing (5.1) and (5.2) into (3.2) at the interior points (test points) \mathbf{x}_i , $i = 1, \dots, N_I$ gives

$$\begin{aligned}
\sum_{j \in I(\mathbf{x}_i)} w_j(\mathbf{x}_i) \frac{d\varphi_j(t)}{dt} &= \tilde{\lambda} \sum_{j \in I(\mathbf{x}_i)} w_j^L(\mathbf{x}_i) \varphi_j(t) - \frac{1}{\tilde{\tau}} F' \left(\sum_{j \in I(\mathbf{x}_i)} w_j(\mathbf{x}_i) \varphi_j(t) \right) + \tilde{\chi} \sum_{j \in I(\mathbf{x}_i)} w_j(\mathbf{x}_i) \tilde{\sigma}_j(t) \\
&\quad - \tilde{A} \sum_{j \in I(\mathbf{x}_i)} w_j(\mathbf{x}_i) \varphi_j(t), \\
\sum_{j \in I(\mathbf{x}_i)} w_j(\mathbf{x}_i) \frac{d\tilde{\sigma}_j(t)}{dt} &= \tilde{\epsilon} \sum_{j \in I(\mathbf{x}_i)} w_j^L(\mathbf{x}_i) \tilde{\sigma}_j(t) + \tilde{s} - \tilde{\delta} \sum_{j \in I(\mathbf{x}_i)} w_j(\mathbf{x}_i) \varphi_j(t) - \tilde{\gamma} \sum_{j \in I(\mathbf{x}_i)} w_j(\mathbf{x}_i) \tilde{\sigma}_j(t), \\
\sum_{j \in I(\mathbf{x}_i)} w_j(\mathbf{x}_i) \frac{d\tilde{p}_j(t)}{dt} &= \tilde{\eta} \sum_{j \in I(\mathbf{x}_i)} w_j^L(\mathbf{x}_i) \tilde{p}_j(t) + \tilde{\alpha}_h \left(1 - \sum_{j \in I(\mathbf{x}_i)} w_j(\mathbf{x}_i) \varphi_j(t) \right) + \tilde{\alpha}_c \sum_{j \in I(\mathbf{x}_i)} w_j(\mathbf{x}_i) \varphi_j(t) \\
&\quad - \tilde{\gamma}_p \sum_{j \in I(\mathbf{x}_i)} w_j(\mathbf{x}_i) \tilde{p}_j(t),
\end{aligned} \tag{5.3}$$

where the weights $w_j(\mathbf{x}_i)$ and $w_j^L(\mathbf{x}_i)$ are computed by the RBF-FD scheme. In vectorial form (5.3) can be compactly re-written

$$\begin{aligned}
\frac{d\boldsymbol{\varphi}_I}{dt} &= \tilde{\lambda} W_{X_I}^L \boldsymbol{\varphi}_X - \frac{1}{\tilde{\tau}} F'(\boldsymbol{\varphi}_I) + \tilde{\chi} \tilde{\boldsymbol{\sigma}}_I - \tilde{A} \boldsymbol{\varphi}_I, \\
\frac{d\tilde{\boldsymbol{\sigma}}_I}{dt} &= \tilde{\epsilon} W_{X_I}^L \tilde{\boldsymbol{\sigma}}_X + \tilde{s} - \tilde{\delta} \boldsymbol{\varphi}_I - \tilde{\gamma} \tilde{\boldsymbol{\sigma}}_I, \\
\frac{d\tilde{\boldsymbol{p}}_I}{dt} &= \tilde{\eta} W_{X_I}^L \tilde{\boldsymbol{p}}_X + \tilde{\alpha}_h (1 - \boldsymbol{\varphi}_I) + \tilde{\alpha}_c \boldsymbol{\varphi}_I - \tilde{\gamma}_p \tilde{\boldsymbol{p}}_I,
\end{aligned} \tag{5.4}$$

in which

$$\boldsymbol{\varphi}_I = [\varphi_j(t)]_{1 \leq j \leq N_I}, \quad \tilde{\boldsymbol{\sigma}}_I = [\tilde{\sigma}_j(t)]_{1 \leq j \leq N_I}, \quad \tilde{\boldsymbol{p}}_I = [\tilde{p}_j(t)]_{1 \leq j \leq N_I},$$

and

$$W_{X_I}^L = [w_j^L(\mathbf{x}_i)]_{1 \leq i \leq N_I, 1 \leq j \leq N},$$

which is a sparse differentiation matrix thanks to the RBF-FD scheme. The vectors $\boldsymbol{\varphi}_X$, $\tilde{\boldsymbol{\sigma}}_X$ and $\tilde{\boldsymbol{p}}_X$ can be partitioned in $\boldsymbol{\varphi}_X = [\boldsymbol{\varphi}_I \quad \boldsymbol{\varphi}_B]^T$, $\tilde{\boldsymbol{\sigma}}_X = [\tilde{\boldsymbol{\sigma}}_I \quad \tilde{\boldsymbol{\sigma}}_B]^T$ and $\tilde{\boldsymbol{p}}_X = [\tilde{\boldsymbol{p}}_I \quad \tilde{\boldsymbol{p}}_B]^T$, where again the indices I and B show the approximation value of each unknown variable at interior and boundary points, respectively.

Using the fact that the boundary conditions are of Dirichlet type, we can impose them directly in

equations (5.4). In fact, $\varphi_B = 0$, $\tilde{\sigma}_B = 0$ and $\tilde{\rho}_B = 0$. Considering this, we can rewrite (5.4) as follows

$$\begin{aligned}\frac{d\varphi_I}{dt} &= \tilde{\lambda}W_{X_I}^{L,I}\varphi_I - \frac{1}{\tilde{\tau}}F'(\varphi_I) + \tilde{\chi}\tilde{\sigma}_I - \tilde{A}\varphi_I, \\ \frac{d\tilde{\sigma}_I}{dt} &= \tilde{\varepsilon}W_{X_I}^{L,I}\tilde{\sigma}_I + \tilde{s} - \tilde{\delta}\varphi_I - \tilde{\gamma}\tilde{\sigma}_I, \\ \frac{d\tilde{\rho}_I}{dt} &= \tilde{\eta}W_{X_I}^{L,I}\tilde{\rho}_I + \tilde{\alpha}_h(1 - \varphi_I) + \tilde{\alpha}_c\varphi_I - \tilde{\gamma}_p\tilde{\rho}_I,\end{aligned}\tag{5.5}$$

with $W_{X_I}^{L,I} = [w_j^L(\mathbf{x}_i)]_{1 \leq i, j \leq N_I}$.

Finally, (5.5) with the proper initial conditions can be written in matrix form as below

$$\begin{aligned}\frac{d\mathbf{u}_I}{dt} &= B\mathbf{u}_I + F(X_I, t, \mathbf{u}_I), \\ \mathbf{u}_I(0) &= G(X_I, 0),\end{aligned}\tag{5.6}$$

in which $\mathbf{u}_I = [\varphi_I, \tilde{\sigma}_I, \tilde{\rho}_I]_{3N_I \times 1}^T$, B is a sparse matrix with size $3N_I \times 3N_I$ due to (5.6). F is the nonlinear term vector with size $3N_I \times 1$ (cf. (5.5)), and G represents the value of the unknown variables at time $t = 0$ and at interior points X_I . By solving (5.6) at every time step, we can also obtain the approximate value of each variable at the boundary nodes.

6. The fully discretized scheme

We discuss how to solve (5.6) with respect to t . We recall that different approaches can deal with the time discretization of MOL. Just to mention the most commonly used, there are explicit integrators, as the fourth-order Runge-Kutta (RK4) or implicit time integrators, such as the backward differential formulas (BDFs) or SBDFs (cf. e.g. [26, 27, 33, 57, 70]).

As it is well-known, a necessary condition for stability of the MOL is that all eigenvalues of the differentiation matrix B in (5.6), lie in the stability region. In [69], an implicit condition for showing all the eigenvalues of the differentiation matrix (here is called W_X^L) obtained via the augmented (overlapped) RBF-FD method, which lie in the left half complex plane, has been derived. However, until now, there is no theoretical proof on how to derive an explicit condition for this, but we can numerically verify it, by computing all the eigenvalues, for instance by using the MATLAB function `eigs` (which allows a stable computation of all the eigenvalues at once). As an illustrative example, Figure 2 displays the eigenvalues of B for $n = 13$ with $\varepsilon = 15, 20$ and $N_I = 3969, 16129$ and 25281 uniform points (see Section 7). The results show that all eigenvalues of B belong to the left half complex plane (i.e., they have negative real parts) even for a low number N of points. Besides, the imaginary part is in magnitude much smaller than the real part. We also should mention that the choice of n and ε can affect the results. The user should therefore choose these parameters carefully so that the numerical solution be “*acceptable*”, that is not too far from what one expect. In the next section, we show how these two parameters can affect the results and can properly be chosen.

Due to this, in this work, we consider a *SBDF1 algorithm* for discretizing (5.6) in time, so that $B\mathbf{u}_I$ and $F(X_I, t, \mathbf{u}_I)$ are considered as the implicit and the explicit terms, respectively.

We now assume that the time interval $[0, T]$ is divided uniformly into $[t_{k-1}, t_k]$, $k = 1, \dots, M$ (i.e., M sub-intervals), where $t_0 = 0$, $t_k = k\Delta t$ for $k = 1, \dots, M$ and $\Delta t = T/M$, is the time step.

Applying the SBDF1 method to the MOL (5.6) gives

$$(I - \Delta t B)\mathbf{U}_I^{n+1} = \mathbf{U}_I^n + \Delta t F(X_I, t^n, \mathbf{U}_I^n), \quad n = 0, 1, \dots, M - 1, \quad (6.1)$$

where I is the identity matrix of order $3N_I$, \mathbf{U}_I^{n+1} is the vector of approximation values of the unknowns at $t = t_{k+1} := (k+1)\Delta t$ and at the X_I points. By computing the approximation value of each variable at X_I , by using (6.1), the approximation of φ , $\tilde{\sigma}$ and \tilde{p} can be obtained at X_B , at any time step. Using these values, the approximated solution of φ , σ and p will be computed at an arbitrary node $\mathbf{x} \in \Omega$ thanks to (5.1).

Remark 6.1. *The fully discretized scheme (6.1) is a linear system of algebraic equations that has to be solved at each time step. For this issue, we have applied the BiCGSTAB method with zero-fill ILU as preconditioner [73]. We notice that many authors successfully applied this approach to solve the linear system of algebraic equations arising from the discretization of time-dependent PDEs via meshless techniques in space and explicit, implicit, semi-implicit approaches in time (cf. e.g. [17, 58, 47, 60]).*

7. Results

We present some simulation of the non-dimensional model (3.2) to show the prostate tumor growth in two-dimensional domains: in a rectangle and in a circle. For the results presented here, two sets of nodes are considered: *uniform* and *quasi-uniform*. **Both sets can** easily be generated by MATLAB functions. The uniform ones by the function `meshgrid` available in the standard MATLAB distribution, while the quasi-uniform nodes by the package `distmesh` (see [62]), which is widely used in solving PDEs problem. The package is freely available at the website: <https://popersson.github.io/distmesh/>.

Using the definition (4.1), to find n nearest points (the size of local domain of influence) around each point of X we use another MATLAB function: `knnsearch`. With this, we can construct the differentiation matrix $W_{X_I}^{L,I}$ by using, for instance, MQ radial basis function with $\beta = 1/2$ (see the third row of Table 2)

$$\phi(r) = \sqrt{1 + \varepsilon^2 r^2}, \quad (7.1)$$

with $r := \|\mathbf{x} - \mathbf{y}\|_2$, $\mathbf{x}, \mathbf{y} \in \Omega$. All figures presented in this section are drawn with the fixed shape parameter $\varepsilon = 15$. We recall that for finding a proper or optimal shape parameter ε^* , interested readers can refer, for instance, to [24, 63], but here, we will not discuss this issue.

The sparsity pattern of the matrix W_X^L is drawn in Figure 3 for a fixed value of $N = 25921$ uniform points and $n = 13, 17, 21$ and 31 . Besides, the approximate percentage of non-zero (nz) elements of the matrix W_X^L are reported in Table 3 for the chosen values of n and N .

n	$N = 6561$	$N = 25921$	$N = 103041$
13	20%	5%	1.3%
17	26%	6.6%	1.6%
21	32%	8.1%	2%
31	47%	12%	3%

Table 3: The approximate percentage of non-zero (nz) elements of the matrix W_X^L for different values of n and N .

The time step is chosen as $\Delta t = 1e - 4$ due to the time discretization proposed here. In order to apply the BiCGSTAB method for solving the linear system (6.1) at each time step, the tolerance and the maximum number of iterations are fixed as $\text{tol} = 1e - 6$ and $\text{maxit} = 100$, respectively.

Remark: *the results presented here are obtained with iterations ≤ 2 for all chosen N . The numerical experiments have been done in MATLAB 2017a using standard double precision, on a PC Core i7 – 2670QM with 8 GB of RAM.*

7.1. Results on rectangular and circular domains

Here we provide some numerical simulations to show the prostate tumor growth in the two-dimensional space. Due to the non-dimensionalization technique given in Section 3, we have some freedom in the choice of the domains. We have then taken the rectangular domain $\Omega = [0, 2]^2$ and the circular domain $\Omega = \{(x, y) \in \Omega : (x - 1)^2 + (y - 1)^2 \leq 1\}$. For these simulations, the constant parameters given in Table 1 are used in non-dimensional form. Following [51], the initial condition function φ , is taken to be

$$\varphi(x, y, 0) = \begin{cases} 1, & \frac{(x-1)^2}{(0.1)^2} + \frac{(y-1)^2}{(0.15)^2} \leq 1, \\ 0, & \text{otherwise} \end{cases} \quad (7.2)$$

while the initial conditions for $\tilde{\sigma}$ and \tilde{p} are set to be zero.

We note that the exact solution of the problem is not known, so to measure the accuracy of the method we use the following strategy:

- as exact solution we consider the approximate solution at $N = 410881$ uniform points, $n = 60$, $\varepsilon = 35$ and constant time step, i.e., $\Delta t = 1e - 4$;
- the maximum relative error, e_∞ is computed for different values of N , where

$$e_\infty := \frac{\|u_{ex} - u_{app}\|_\infty}{\|u_{ex}\|_\infty}, \quad (7.3)$$

in which u_{ex} and u_{app} denote the **exact and approximate solutions**, respectively, which are computed on $26400 = 220 \times 120$ evenly spaced point grid of $[0, 2]^2$ and $\|\cdot\|_\infty$ represents the usual maximum norm.

In Table 4, we report the maximum relative errors for φ , $\tilde{\sigma}$ and \tilde{p} together with the CPU time at $t = 1e-2$ via different values of N , for $n = 13$ and $\varepsilon = 26$.

N	$e_{\infty, \varphi}$	$e_{\infty, \tilde{\sigma}}$	$e_{\infty, \tilde{p}}$	CPU time(s)
6561	$1.91e + 0$	$5.59e - 1$	$9.12e - 1$	9.041
25921	$2.00e - 1$	$3.56e - 2$	$1.26e - 1$	18.860
103041	$1.86e - 2$	$4.72e - 3$	$1.19e - 2$	97.085

Table 4: The errors $e_{\infty, *}$, $'*'$ = $\varphi, \tilde{\sigma}, \tilde{p}$, the CPU time at $t = 1e - 2$, $n = 13$ $\varepsilon = 26$, for different N .

To show the effect of the choice of the shape parameter on the accuracy and the rate of convergence of the RBF-FD scheme, we have fixed $n = 13$ and used $\varepsilon = 15, 20$ and 25 . The maximum relative errors are computed for φ , $\tilde{\sigma}$ and \tilde{p} in Figure 4. From this figure, we can see that by increasing the value of shape parameter, the accuracy of the RBF-FD method is improving giving almost the same rate of convergence. Furthermore, the condition number of the matrix W_X^L is computed for different values of ε and values are displayed in Table 5. According to the results of Table 5, it is clear that on different N when the value of

N	$\varepsilon = 10$	$\varepsilon = 15$	$\varepsilon = 20$	$\varepsilon = 25$
6561	$3.03e + 7$	$3.41e + 5$	$2.06e + 5$	$1.10e + 5$
25921	$4.25e + 9$	$5.61e + 7$	$1.23e + 8$	$2.62e + 6$
103041	$1.72e + 11$	$2.57e + 10$	$2.92e + 10$	$8.96e + 8$

Table 5: The condition number of the matrix W_X^L with different values of ε and N , fixed $n = 13$.

shape parameter increases the condition number of W_X^L decreases, as expected by the trade-off principle.

In addition, we have fixed the shape parameter $\varepsilon = 25$, and we have computed the maximum relative errors for φ , $\tilde{\sigma}$ and \tilde{p} via $n = 17, 21$ and 25 . The results are reported in Figure 5. This figure also shows that when the number of points in each stencil has been increased the accuracy of the method is slowly improving. Of course, it certainly depends on **the choice of the shape parameter**.

In Figure 6, the initial condition and the numerical solution of the tumor phase field φ are provided at different time steps $t = 0.2, 0.4$ and 0.6 by using $N = 16641$ uniform nodes. The same results are given in Figure 7 with $N = 66049$ uniform nodes. The results agree with those reported in [50, 51]. To see the steady-state solution of our dimensionless model with the parameters given in Table 1, we wrote a MATLAB program, supplied in GitHub (available at the link <https://github.com/VM-2020-MATH/MATLAB-codes-for-the-Prostate-Tumor-Growth.git>, the program `Main_PCa_RBF_FD.m`) that has been run until $\|\Phi^{n+1} - \Phi^n\|_{\infty} < 10^{-6}$, $\|\tilde{\sigma}^{n+1} - \tilde{\sigma}^n\|_{\infty} < 10^{-6}$ and $\|\tilde{p}^{n+1} - \tilde{p}^n\|_{\infty} < 10^{-6}$. The steady-state solutions of φ , $\tilde{\sigma}$ and \tilde{p} are presented in Figure 8.

To show the capability of our numerical meshless method, we did the same simulations with $N = 17799$ quasi-uniform nodes generated by `distmesh` with the boundary nodes distributed uniformly and fixed shape parameter $\varepsilon = 10$. The results are shown in Figure 9.

On the circular domain, we used the same initial conditions as for the rectangular case. Figure 10

shows the approximate solution of φ at different time steps using $N = 11027$ uniform nodes (generated by `distmesh`) in which the boundary nodes are distributed uniformly. In Figure 11, the results are those obtained using $N = 22999$ uniform nodes, with uniformly distributed boundary nodes.

In Figure 12, we report the simulation results of the prostate **tumor growth on a circular domain** with $N = 21077$ quasi-uniform nodes with the boundary nodes distributed uniformly. The numerical solution of tumor phase field φ , is plotted at different time steps $t = 0.2, 0.4$ and 0.6 .

7.2. Results based on parameters seen in clinical practice and experiments

Here we present some simulations, which are obtained using the parameters observed experimentally in [50]. The diffusion coefficient of the phase field, λ and nutrient diffusivity ϵ , were measured and their values are $5 \times 10^{-11} \text{ cm}^2/\text{s}$ and $2 \times 10^{-9} \text{ cm}^2/\text{s}$, respectively. To show the effect of choosing different values of the nutrient supply s , the numerical results have been obtained taking the values $2.60 \text{ g}/(L \cdot \text{day})$, $2.70 \text{ g}/(L \cdot \text{day})$ and $2.80 \text{ g}/(L \cdot \text{day})$, as indicated in [50]. Other parameters are fixed as in Table 1. The number of nodes, uniformly distributed in the rectangular domain, is $N = 25921$. The numerical solutions of the prostate tumor growth, the nutrient and PSA are drawn at different time levels with $s = 2.60 \text{ g}/(L \cdot \text{day})$ in Figure 13, $s = 2.70 \text{ g}/(L \cdot \text{day})$ in Figure 14 and $s = 2.80 \text{ g}/(L \cdot \text{day})$ in Figure 15. As can be observed the *fingered morphology grows with thinner and less branches* when $s = 2.60 \text{ g}/(L \cdot \text{day})$ (i.e., nutrient supply is reduced). By increasing the value of the nutrient supply to $s = 2.80 \text{ g}/(L \cdot \text{day})$, wider branches have been produced in the fingered morphology of the prostate tumor growth. It also can be observed that when the value of s is low, the growth of tumor is slow, but by increasing this value up to 2.80 makes the tumor grows at a faster rate (see also supplementary movies).

In addition, the results obtained here and those reported in [50], show that the tumor initially grows spherically. If the tumor keeps developing on with this morphology, it consumes more nutrients and thus the nutrient concentration will be decreased, which makes hypoxia, starvation, and necrosis. Finally, the tumor reaches a volume such that it changes to the displayed fingered morphology. As pointed out in [50], the nutrient concentration within the tumor is not important at all, see Figure 15.

Figure 16 shows the values of tumor volume (formula (2.2) in μm^3 and serum PSA, (formula (2.5)) in ng/ml , at different time levels. Furthermore, the steady-state solutions of φ , $\tilde{\sigma}$ and \tilde{p} are given in Figure 17 for $s = 2.80 \text{ g}/(L \cdot \text{day})$ (see the details given in Subsection 7.1).

To show the simulation results that can support the experimental results in [41], we used $s = (2.75 + c) \text{ g}/(L \cdot \text{day})$ as nutrient supply, where c is a mild heterogeneity (due to vasculature) such that s changes between $2.55 \text{ g}/(L \cdot \text{day})$ (far from the blood vessels) and $2.95 \text{ g}/(L \cdot \text{day})$ (near the blood vessels). This choice is a more realistic distribution in the nutrient supply for a tissue domain, as pointed out in [50]. We then used the following initial conditions for the nutrient and PSA [9].

$$\tilde{\sigma}(x, y, 0) = c_{\tilde{\sigma}}^0 + c_{\tilde{\sigma}}^1 \phi(x, y, 0), \quad (7.4)$$

$$\tilde{p}(x, y, 0) = c_{\tilde{p}}^0 + c_{\tilde{p}}^1 \phi(x, y, 0), \quad (7.5)$$

where $c_{\tilde{\sigma}}^0 = 1$, $c_{\tilde{\sigma}}^1 = -0.8$, $c_{\tilde{p}}^0 = 6.2500 \times 10^{-8}$, $c_{\tilde{p}}^1 = 7.9750 \times 10^{-7}$ are chosen in non-dimensional form. Figure 18 illustrates the numerical solutions of the prostate tumor growth, the nutrient and PSA using

$N = 25961$ uniform nodes. The fingered tumor growth pattern, which was observed in vitro 3D Matrigel culture of RWPE-1 cells [41], can be seen in this simulation, as well.

8. Conclusion and the future work

A non-dimensional form of the mathematical model for the prostate tumor growth has been derived. **It makes it** easy to apply different numerical methods for solving this model which arise in oncology. In this paper, a meshless technique, namely RBF-FD method in space and a semi-implicit approach based on SBDF1 formulas in time, have been successfully applied to solve it numerically on rectangular and circular regions, with uniform and quasi-uniform node distributions. We have shown that the method is numerically accurate and stable. Some numerical simulations have been done on clinical data borrowed from the literature, with results in agreement with those reported in the literature. The main advantages of the proposed numerical scheme are:

- Its implementation is simpler than the mesh-dependent methods. In fact, the differentiation matrix (which is a sparse matrix) is constructed at the scattered nodes without using a background mesh or triangulation (as given in Section 4).
- When different types of distribution nodes are used to construct the differentiation matrix in the rectangular and circular domains no new implementation is needed.
- **The meshless nature** of our approach allows **us to easily implement it** on rectangular or circular regions simply by the use of two different node distributions, uniform, and quasi-uniform.
- All simulations done can also be obtained by increasing the number of nodes in each local domain of influence, by changing n . Of course, the computational cost will be increased but not significantly.
- Unlike the methods of [50, 51], it is not necessary to use any adaptivity algorithms for solving this mathematical model.
- As we have mentioned in this paper, it is possible to apply different algorithms for finding a proper shape parameter.
- Although this method can be implemented in higher dimensions, the computational cost will be increased dramatically. On the other side, we had no access to fast and powerful computers, so that we were not able to get, for instance, three-dimensional results. We can access to clusters, or we can do parallel computing in the future.

Supplementary movies

The process of tumor phase field, nutrient and the prostate specific antigen in two-dimensional tissue are provided for $N = 25961$ uniform nodes, with supply nutrient $s = 2.80 \text{ g}/(L \cdot \text{day})$ in three separate movies, downloadable at the link

<https://github.com/VM-2020-MATH/Simulation-Prostate-Tumor-Growth-RBF-FD-Scheme>.

Acknowledgments. The third author has been supported by the GNCS-INdAM and the University of Padova DOR2018 funds. This research has been accomplished with the auspices of RITA, Italian Network on Approximation. The authors are very grateful to the reviewers for carefully reading this paper and for their comments and suggestions, which have significantly improved the paper.

References

- [1] Simulation flows with multiple phases and components via the radial basis functions-finite difference (RBF-FD) procedure: Shan-Chen model, *Engineering Analysis with Boundary Elements*, 119 (2020) 151-161.
- [2] V. Andasari, Mathematical modelling of cancer cell invasion of tissue: discrete and continuum approaches to studying the central role of adhesion, Ph.D. thesis, University of Dundee, 2011.
- [3] A. R. Anderson, M. A. J. Chaplain, Continuous and discrete mathematical models of tumor-induced angiogenesis, *Bulletin of Mathematical Biology*, 60 (5) (1998) 857-899.
- [4] A. R. Anderson, M. A. Chaplain, E. L. Newman, R. J. Steele, A. M. Thompson, Mathematical modelling of tumour invasion and metastasis, *Computational and Mathematical Methods in Medicine*, 2 (2) (2000) 129-154.
- [5] V. Bayona, N. Flyer, B. Fornberg, G. A. Barnett, On the role of polynomials in RBF-FD approximations: II. Numerical solution of elliptic PDEs, *J. Comput. Phys.*, 332 (2017) 257-273.
- [6] V. Bayona, An insight into RBF-FD approximations augmented with polynomials, *Computer & Mathematics with Applications*, 77 (2019) 2337-2353.
- [7] V. Bayona, Comparison of moving least squares and RBF+poly for interpolation and derivative approximation, *Journal of Scientific Computing*, 81 (2019) 486-512.
- [8] P. Ciarletta, L. Foret, M. Ben Amar, The radial growth phase of malignant melanoma: multi-phase modelling, numerical simulations and linear stability analysis, *Journal of the Royal Society Interface*, 8 (56) (2011) 345-368.
- [9] P. Colli, H. Gomez, G. Lorenzo, G. Marinoschi, A. Reali, E. Rocca, Mathematical analysis and simulation study of a phase-field model of prostate cancer growth with chemotherapy and antiangiogenic therapy effects, *Mathematical Models and Methods in Applied Sciences*, 30 (07) (2020) 1253-1295.
- [10] G. M. Cooper, R. E. Hausman, The development and causes of cancer, *The cell: A molecular approach*, (2000) 725-766.
- [11] O. Davydov, R. Schaback, Error bounds for kernel-based numerical differentiation, *Numerische Mathematik*, 132 (2) (2016) 243-269.

- [12] O. Davydov, R. Schaback, Minimal numerical differentiation formulas, *Numerische Mathematik*, 140 (3) (2018) 555-592.
- [13] O. Davydov, R. Schaback, Optimal stencils in Sobolev spaces, *IMA Journal of Numerical Analysis*, 39 (1) (2019) 398–422.
- [14] M. Dehghan, V. Mohammadi, The method of variably scaled radial kernels for solving two-dimensional magnetohydrodynamic (MHD) equations using two discretizations: The Crank-Nicolson scheme and the method of lines (MOL), *Comput. Appl. Math.* 70 (2015) 2292-2315.
- [15] M. Dehghan, V. Mohammadi, A numerical scheme based on radial basis function finite difference (RBF-FD) technique for solving the high-dimensional nonlinear Schrödinger equations using an explicit time discretization: Runge-Kutta method, *Computer Physics Communications*, 217 (2017) 23-34.
- [16] M. Dehghan, N. Narimani, An element-free Galerkin meshless method for simulating the behavior of cancer cell invasion of surrounding tissue, *Applied Mathematical Modelling*, 59 (2018) 500-513.
- [17] M. Dehghan, N. Narimani, The element-free Galerkin method based on moving least squares and moving Kriging approximations for solving two-dimensional tumor-induced angiogenesis model, *Engineering with Computers*, 36 (2020) 1517-1537.
- [18] M. Dehghan, V. Mohammadi, Two-dimensional simulation of the damped Kuramoto-Sivashinsky equation via radial basis function-generated finite difference scheme combined with an exponential time discretization, *Engineering Analysis with Boundary Elements*, 107 (2019) 168-184.
- [19] M. Dehghan, M. Abbaszadeh, The use of proper orthogonal decomposition (POD) meshless RBF-FD technique to simulate the shallow water equations, *Journal of Computational Physics*, 351(2017) 478–510.
- [20] S. De Marchi, A. Martínez, E. Perracchione, Fast and stable rational RBF-based partition of unity interpolation, *Journal of Computational and Applied Mathematics*, 349 (2019) 331-343.
- [21] S. De Marchi, A. Martínez, E. Perracchione, M. Rossini, RBF-based partition of unity methods for elliptic PDEs: Adaptivity and stability issues via variably scaled kernels, *Journal of Scientific Computing*, 79 (1) (2019) 321-344.
- [22] S. De Marchi, F. Marchetti, E. Perracchione, Jumping with variably scaled discontinuous kernels (VSDKs), *BIT Numerical Mathematics* (2019) 1-23.
- [23] P. Domschke, D. Trucu, A. Gerisch, M. A. Chaplain, Mathematical modelling of cancer invasion: implications of cell adhesion variability for tumour infiltrative growth patterns, *Journal of Theoretical Biology*, 361 (2014) 41-60.
- [24] G. E. Fasshauer, *Meshfree Approximation Methods with MATLAB*, Vol. 6, World Scientific, 2007.

- [25] G. E. Fasshauer, M. J. McCourt, Stable evaluation of Gaussian RBF interpolants, *SIAM Journal of Scientific Computing*, 34 (2) (2012) A737A762.
- [26] N. Flyer, E. Lehto, S. Blaise, G. B. Wright, A. St-Cyr, A guide to RBF-generated finite differences for nonlinear transport: Shallow water simulations on a sphere, *Journal of Computational Physics*, 231 (11) (2012) 4078-4095.
- [27] N. Flyer, G. A. Barnett, L. J. Wicker, Enhancing finite differences with radial basis functions: experiments on the Navier–Stokes equations, *Journal of Computational Physics*, 316 (2016) 39-62.
- [28] B. Fornberg, G. Wright, Stable computation of multiquadric interpolants for all values of the shape parameter, *Computers & Mathematics with Applications*, 48 (2004) 853867.
- [29] B. Fornberg, C. Piret, A stable algorithm for flat radial basis functions on a sphere, *SIAM Journal of Scientific Computing*, 30 (1) (2007) 6080.
- [30] B. Fornberg, E. Larsson, N. Flyer, Stable computations with Gaussian radial basis functions, *SIAM Journal of Scientific Computing*, 33 (2011) 869892.
- [31] B. Fornberg, E. Lehto, Stabilization of RBF-generated finite difference methods for convective PDEs, *Journal of Computational Physics*, 230 (2011) 22702285.
- [32] B. Fornberg, E. Lehto, C. Powell, Stable calculation of Gaussian-based RBF-FD stencils, *Computers & Mathematics with Applications*. 65 (4) (2013) 627-637.
- [33] B. Fornberg, N. Flyer, A primer on radial basis functions with applications to the geosciences, SIAM, 2015.
- [34] H. B. Frieboes, J. S. Lowengrub, S. Wise, X. Zheng, P. Macklin, E. L. Bearer, V. Cristini, Computer simulation of glioma growth and morphology, *Neuroimage*, 37 (2007) S59-S70.
- [35] H. B. Frieboes, F. Jin, Y.-L. Chuang, S. M. Wise, J. S. Lowengrub, V. Cristini, Three-dimensional multispecies nonlinear tumor growth II: tumor invasion and angiogenesis, *Journal of Theoretical Biology*, 264 (4) (2010) 1254-1278.
- [36] A. Gerisch, M. A. J. Chaplain, Mathematical modelling of cancer cell invasion of tissue: local and non-local models and the effect of adhesion, *Journal of Theoretical Biology*, 250 (4) (2008) 684–704.
- [37] H. Gomez, K. G. van der Zee, Computational phase-field modeling, *Encyclopedia of Computational Mechanics Second Edition*, 1-35, 2018.
- [38] A. Gierer, H. Meinhardt, A theory of biological pattern formation, *Kybernet.* 12 (1972) 30-39.
- [39] P. Gray, S. K. Scott, Autocatalytic reactions in the isothermal, continuous stirred tank reactor: isolas and other forms of multistability, *Chem. Eng. Sci.* 38 (1983) 29-43.

- [40] A. Hawkins–Daarud, K. G. van der Zee, J. Tinsley Oden, Numerical simulation of a thermodynamically consistent four–species tumor growth model, *International Journal for Numerical Methods in Biomedical Engineering*, 28 (1) (2012) 3-24.
- [41] V. Härmä, J. Virtanen, R. Mäkelä, A. Happonen, J-P. Mpindi, M. Knuuttila, P. Kohonen, J. Lötjönen, O. Kallioniemi, M. Nees, A comprehensive panel of three–dimensional models for studies of prostate cancer growth, invasion and drug responses, *Plos One*, 5 (5) (2010) e10431.
- [42] S. U. Islam, A. Ali, S. Haq, A computational modeling of the behavior of the two-dimensional reaction-diffusion Brusselator system, *Applied Mathematical Modelling*, 34 (2010) 3896-3909.
- [43] M. Jabalameli, D. Mirzaei, A weak–form RBF–generated finite difference method, *Computers & Mathematics with Applications*, 79 (9) (2020) 2624-2643.
- [44] E. J. Kansa, Multiquadrics–A scattered data approximation scheme with applications to computational fluid-dynamics–I surface approximations and partial derivative estimates, *Computers & Mathematics with Applications*, 19 (8-9) (1990) 127-145.
- [45] E. Larsson, E. Lehto, A. R. H. Heryudono, B. Fornberg, Stable computation of differentiation matrices and scattered node stencils based on Gaussian radial basis functions, *SIAM Journal of Scientific Computing*, 35 (4) (2013) A2096-A2119.
- [46] H. G. Lee, Y. Kim, J. Kim, Mathematical model and its fast numerical method for the tumor growth, *Mathematical Biosciences & Engineering*, 12 (6) (2015) 1173-1187.
- [47] E. Lehto, V. Shankar, G. B. Wright, A radial basis function (RBF) compact finite difference (FD) scheme for reaction-diffusion equations on surfaces, *SIAM Journal on Scientific Computing*, 39 (5) (2017) A2129-A2151.
- [48] I. Lengyel, I. R. Epstein, Modeling of Turing structures in the chlorite-iodidemalonic acid-starch reaction system, *Science*, 251 (1991) 650-652.
- [49] J-G. Liu, M. Tang, L. Wang, Z. Zhou, An accurate front capturing scheme for tumor growth models with a free boundary limit, *Journal of Computational Physics*, 364 (2018) 73–94.
- [50] G. Lorenzo, M. A. Scott, K. Tew, T. J. Hughes, Y. J. Zhang, L. Liu, G. Vilanova, H. Gomez, Tissue–scale, personalized modeling and simulation of prostate cancer growth, *Proceedings of the National Academy of Sciences*, 113 (48) (2016) E7663-E7671.
- [51] G. Lorenzo, M. Scott, K. Tew, T. Hughes, H. Gomez, Hierarchically refined and coarsened splines for moving interface problems, with particular application to phase-field models of prostate tumor growth, *Computer Methods in Applied Mechanics and Engineering*, 319 (2017) 515-548.
- [52] G. Lorenzo, T. J. Hughes, P. Dominguez–Frojan, A. Reali, H. Gomez, Computer simulations suggest that prostate enlargement due to benign prostatic hyperplasia mechanically impedes prostate cancer growth, *Proceedings of the National Academy of Sciences*, 116 (4) (2019) 1152-1161.

- [53] D. Mirzaei, R. Schaback, M. Dehghan, On generalized moving least squares and diffuse derivatives, *IMA Journal of Numerical Analysis*, 32 (3) (2012) 983–1000.
- [54] D. Mirzaei, R. Schaback, Solving heat conduction problems by the direct meshless local Petrov–Galerkin (DMLPG) method, *Numerical Algorithms*, 65 (2) (2014) 275–291.
- [55] D. Mirzaei, Direct approximation on spheres using generalized moving least squares, *BIT Numerical Mathematics*, 57 (4) (2017) 1041–1063.
- [56] D. Mirzaei, The direct radial basis function partition of unity (D-RBF-PU) method for solving PDEs, *SIAM Journal on Scientific Computing*, 2020.
- [57] M. Mohammadi, R. Mokhtari, R. Schaback, Simulating the 2D Brusselator system in reproducing kernel Hilbert space, *Comput. Model Eng. Sci.* 101 (2014) 113–138.
- [58] V. Mohammadi, M. Dehghan, Simulation of the phase field Cahn–Hilliard and tumor growth models via a numerical scheme: Element–free Galerkin method, *Computer Methods in Applied Mechanics and Engineering*, 345 (2019) 919–950.
- [59] V. Mohammadi, D. Mirzaei, M. Dehghan, Numerical simulation and error estimation of the time–dependent Allen–Cahn equation on surfaces with radial basis functions, *Journal of Scientific Computing*, 79 (1) (2019) 493–516.
- [60] V. Mohammadi, M. Dehghan, A. Khodadadian, T. Wick, Numerical investigation on the transport equation in spherical coordinates via generalized moving least squares and moving kriging least squares approximations, *Engineering with Computers*, <https://doi.org/10.1007/s00366-019-00881-3>.
- [61] H. Nojavan, S. Abbasbandy, M. Mohammadi, Local variably scaled Newton basis functions collocation method for solving Burgers’ equation, *Applied Mathematics and Computation*, 330 (2018) 23–41.
- [62] P.-O. Persson, G. Strang, A simple mesh generator in MATLAB, *SIAM review*, 46 (2) (2004) 329–345.
- [63] S. A. Sarra, A local radial basis function method for advection–diffusion–reaction equations on complexly shaped domains, *Applied Mathematics and Computation*, 218 (19) (2012) 9853–9865.
- [64] R. Schaback, Error analysis of nodal meshless methods, in: *Meshfree methods for partial differential equations VIII*, Springer, 2017, pp. 117–143.
- [65] E. E. Sel’kov, Self-oscillations in glycolysis, *European Journal of Biochemistry*, 4 (1968) 79–86.
- [66] J. Schnakenberg, Simple chemical reaction system with limit cycle behaviour, *Journal of Theoretical Biology*, 81 (1979) 389–400.

- [67] V. Shankar, G. B. Wright, A. L. Fogelson, R. M. Kirby, A radial basis function (RBF) finite difference method for the simulation of reaction-diffusion equations on stationary platelets within the augmented forcing method, *International Journal for Numerical Methods in Fluids*, 75 (1) (2014) 1-22.
- [68] V. Shankar, G. B. Wright, R. M. Kirby, A. L. Fogelson, A radial basis function (RBF)-finite difference (FD) method for diffusion and reaction-diffusion equations on surfaces, *Journal of scientific computing* 63 (3) (2015) 745-768.
- [69] V. Shankar, The overlapped radial basis function-finite difference (RBF-FD) method: A generalization of RBF-FD, *Journal of Computational Physics*, 342 (2017) 211-228.
- [70] V. Shankar, A. L. Fogelson, Hyperviscosity-based stabilization for radial basis function-finite difference (RBF-FD) discretizations of advection-diffusion equations, *Journal of Computational Physics*, 372 (2018) 616-639.
- [71] V. Shankar, A. Narayan, R. M. Kirby, RBF-LOI: Augmenting radial basis functions (RBFs) with least orthogonal interpolation (LOI) for solving PDEs on surfaces, *Journal of Computational Physics*, 373 (2018) 722-735.
- [72] C. Shu, H. Ding, K.S. Yeo, Local radial basis function-based differential quadrature method and its application to solve two-dimensional incompressible Navier-Stokes equations, *Computer Methods in Applied Mechanics and Engineering*, 192 (2003) 941-954.
- [73] G. L. Sleijpen, D. R. Fokkema, BiCGstab (l) for linear equations involving unsymmetric matrices with complex spectrum, *Electronic Transactions on Numerical Analysis*, 1 (11) (1993) 2000.
- [74] M. Tillenius, E. Larsson, E. Lehto, N. Flyer, A scalable RBF-FD method for atmospheric flow, *Journal of Computational Physics*, 298 (2015) 406-422.
- [75] A. I. Tolstykh, On using RBF-based differencing formulas for unstructured and mixed structured-unstructured grid calculations, in: *Proceedings of the 16th IMACS world congress*, Vol. 228, Lausanne, 2000, pp. 4606-4624.
- [76] N. Trask, M. Maxey, X. Hu, Compact moving least squares: an optimization framework for generating high-order compact meshless discretizations, *Journal of Computational Physics*, 326 (2016) 596-611.
- [77] P. C. Walsh, J. F. Worthington, *Dr. Patrick Walsh's guide to surviving prostate cancer*, Grand Central Life & Style, 2010.
- [78] H. Wendland, *Scattered Data Approximation*, Cambridge University Press, 2004.
- [79] S. M. Wise, J. S. Lowengrub, H. B. Frieboes, V. Cristini, Three-dimensional multispecies nonlinear tumor growth I: model and numerical method, *Journal of Theoretical Biology*, 253 (3) (2008) 524-543.
- [80] S. M. Wise, J. S. Lowengrub, V. Cristini, An adaptive multigrid algorithm for simulating solid tumor growth using mixture models, *Mathematical and Computer Modelling*, 53 (1-2) (2011) 1-20.

- [81] G. B. Wright, B. Fornberg, Scattered node compact finite difference–type formulas generated from radial basis functions, *Journal of Computational Physics*, 212 (1) (2006) 99-123.
- [82] G.B. Wright, B. Fornberg, Stable computations with flat radial basis functions using vector-valued rational approximations, *Journal of Computational Physics*, 331 (2017) 137156.
- [83] J. Xu, G. Vilanova, H. Gomez, A mathematical model coupling tumor growth and angiogenesis, *PLoS one*, 11 (2) (2016).

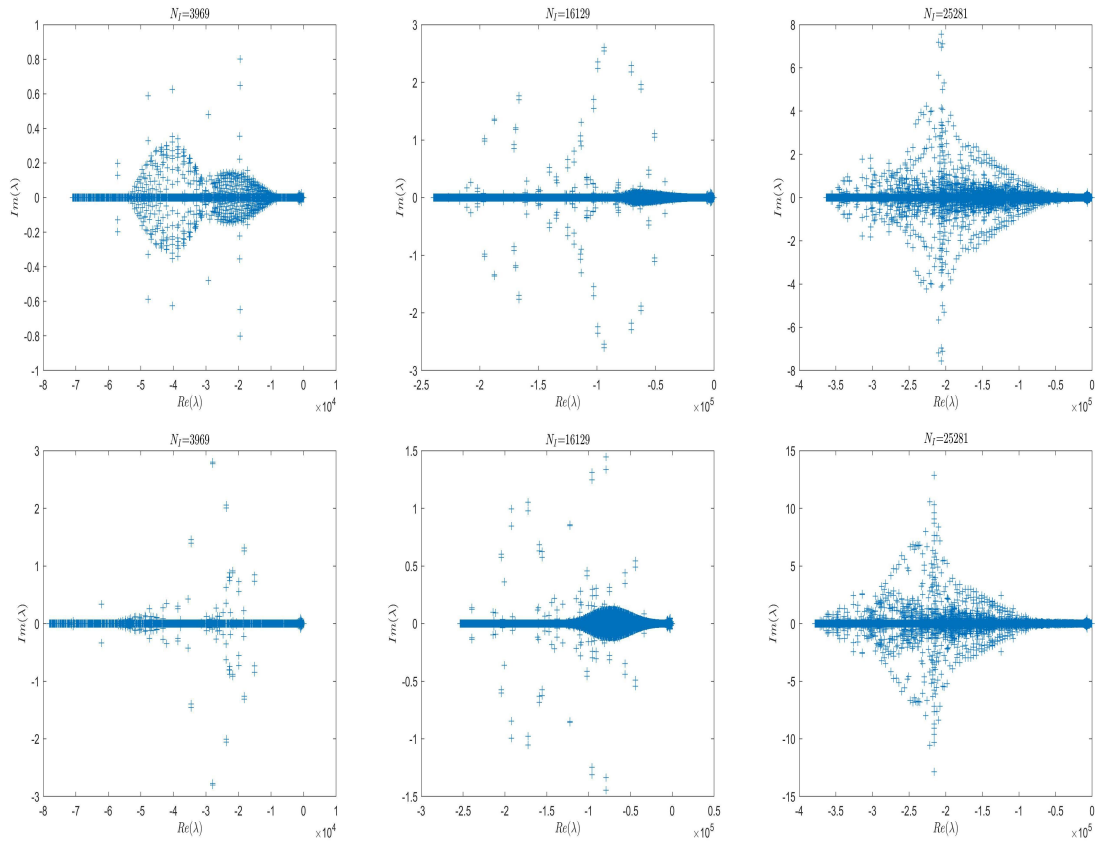


Figure 2: The eigenvalues of B with $n = 13$ and uniform points $N_I = 3969, 16129$ and 25281 . First row: for $\varepsilon = 15$. Second row $\varepsilon = 20$.

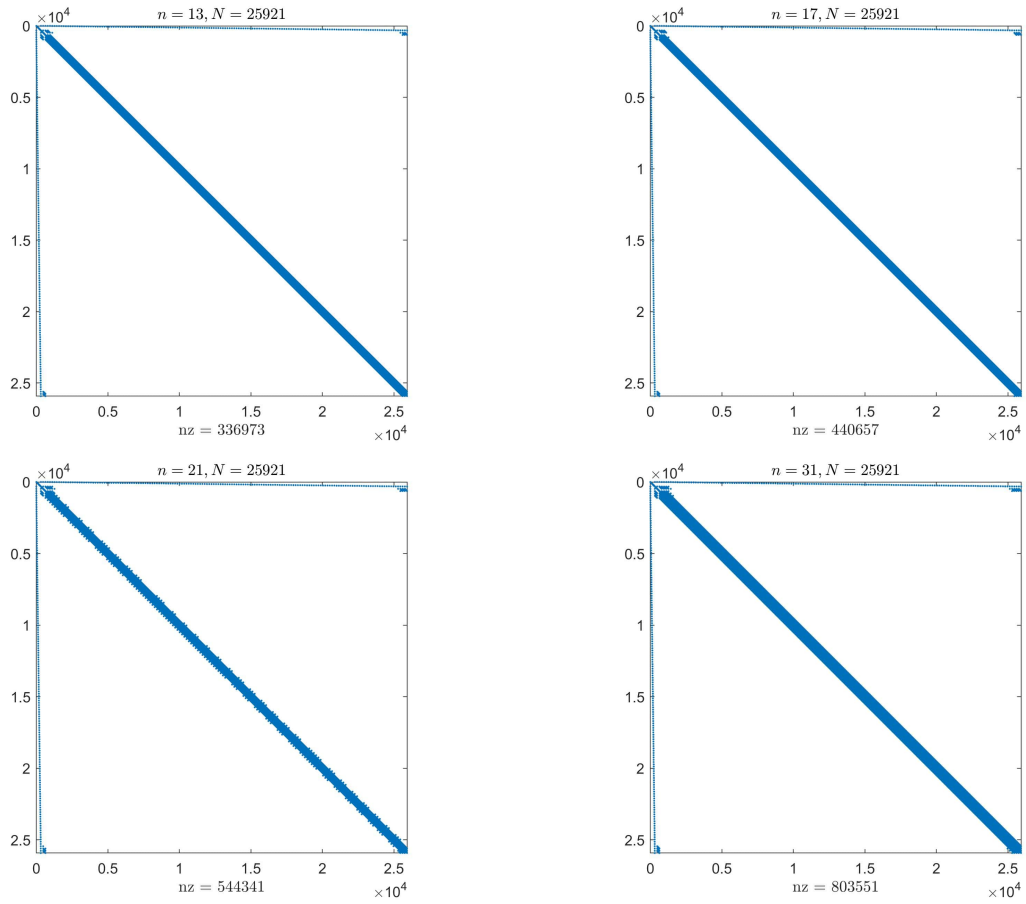


Figure 3: The sparsity pattern of the matrix W_X^L for $N = 25921$ uniform points, $n = 13, 17, 21$ and 31 .

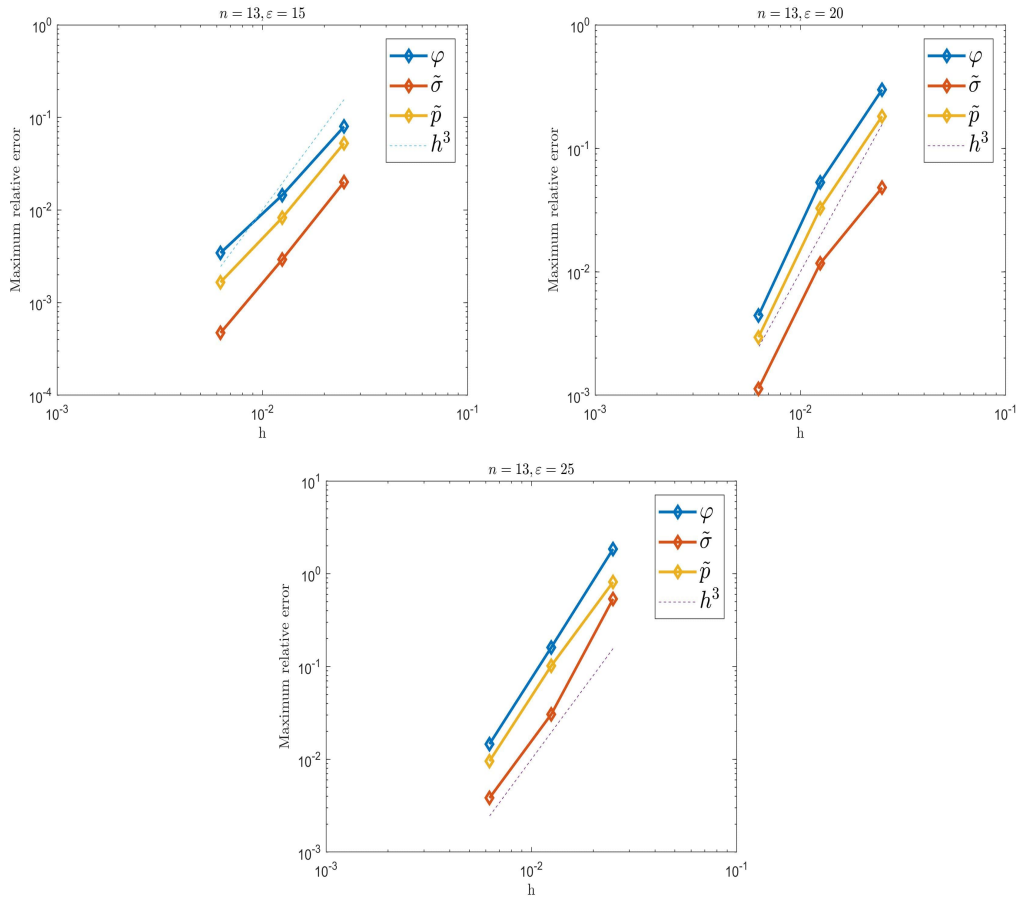


Figure 4: The maximum relative errors for φ , $\tilde{\sigma}$ and \tilde{p} via $n = 13$ and different values of ε . Top left, $\varepsilon = 15$; top right, $\varepsilon = 20$ and bottom, $\varepsilon = 25$.

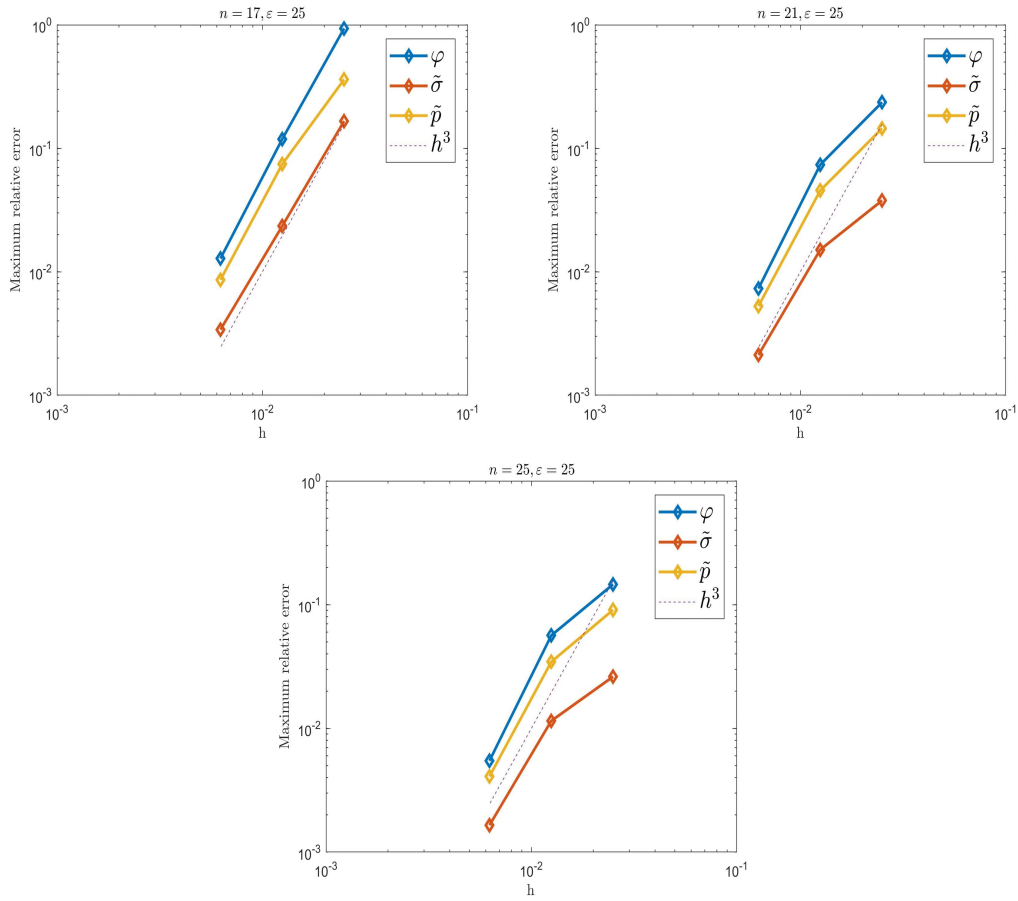


Figure 5: The maximum relative errors for φ , $\tilde{\sigma}$ and \tilde{p} via $\epsilon = 25$ and different values of n . Top left, $n = 17$; right top, $n = 21$ and bottom, $n = 25$.

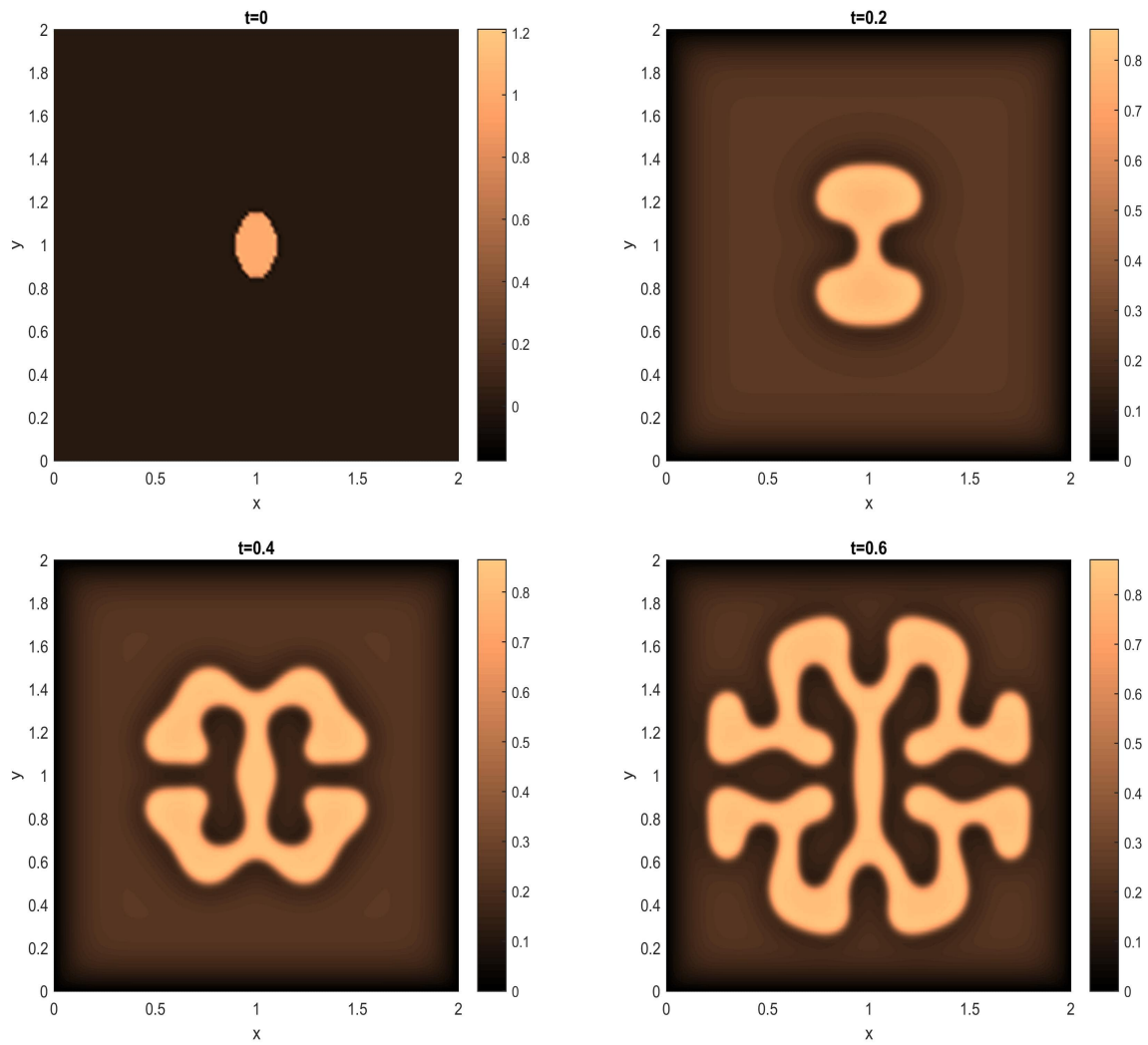


Figure 6: The initial condition and numerical solution of tumor phase field φ at different time levels using $N = 16641$ uniform nodes.

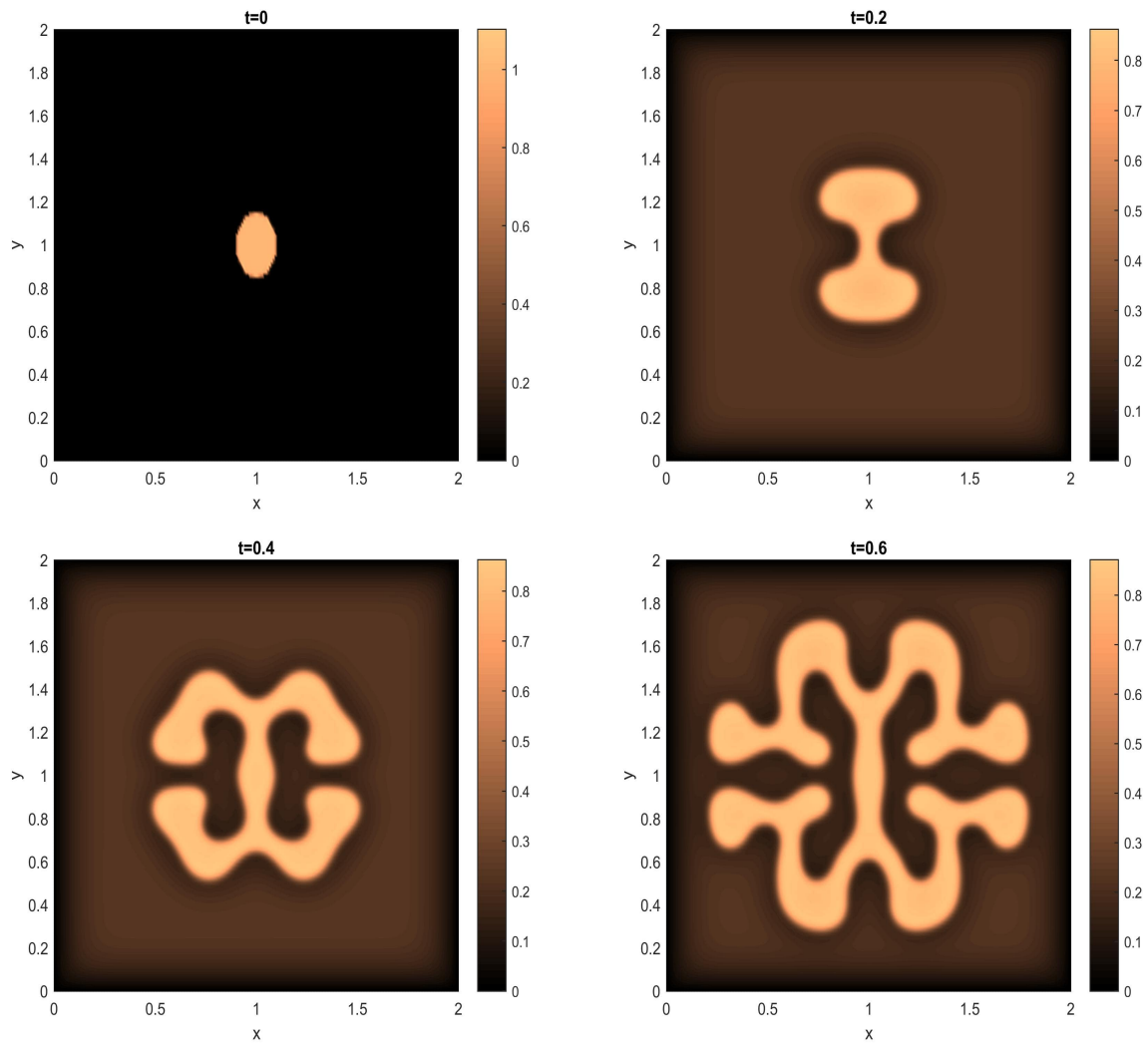


Figure 7: The initial condition and numerical solution of tumor phase field φ at different time levels using $N = 66049$ uniform nodes.

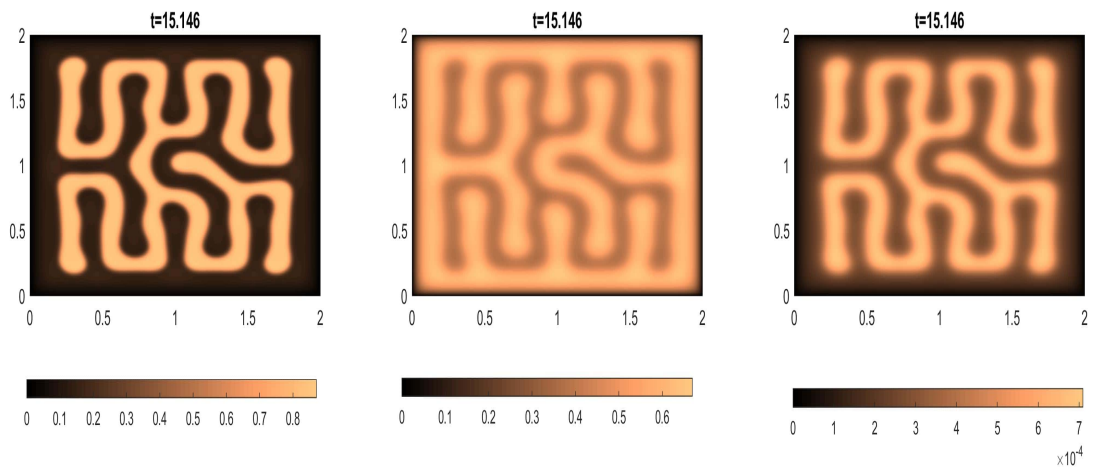


Figure 8: The steady-state solutions of φ , $\tilde{\sigma}$ and \tilde{p} using $N = 25921$ uniform points.

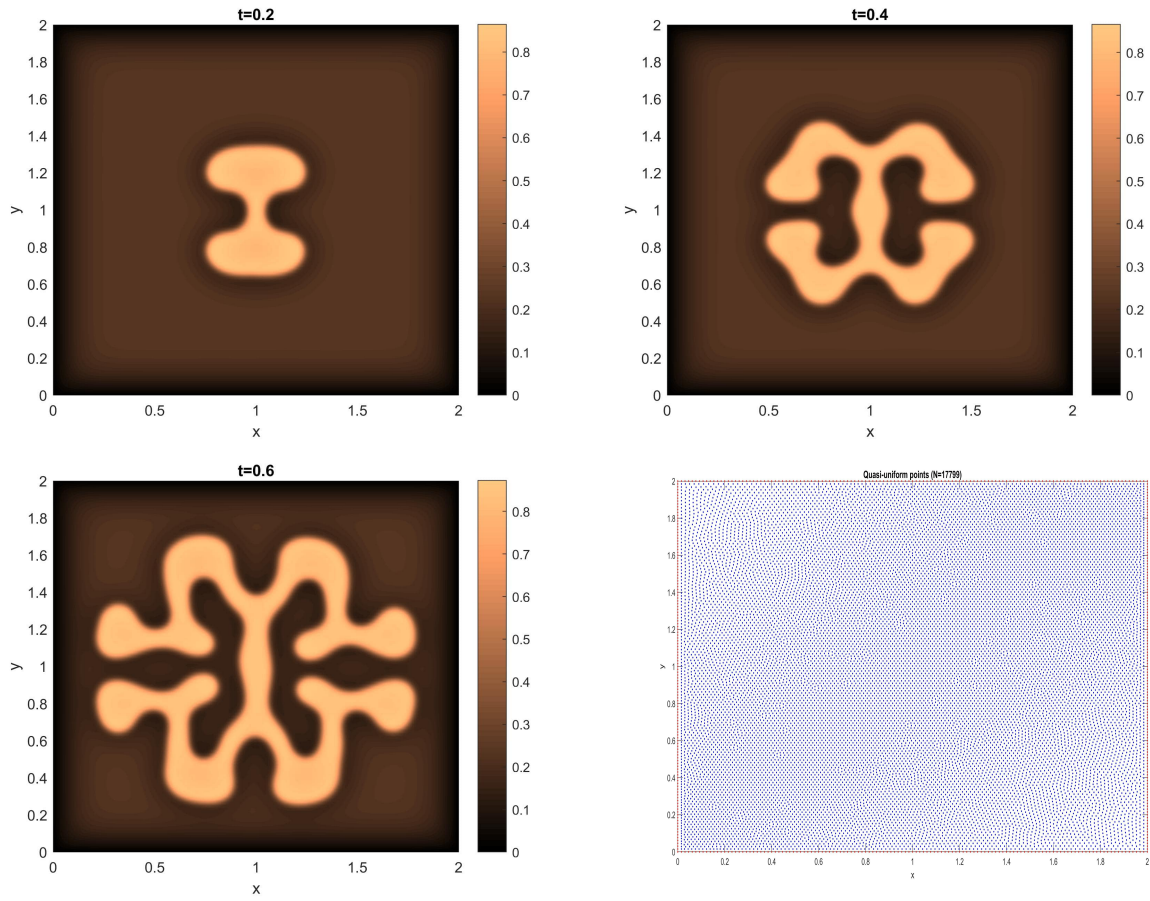


Figure 9: The numerical solution of tumor phase field φ at different time levels using $N = 17799$ quasi-uniform nodes.

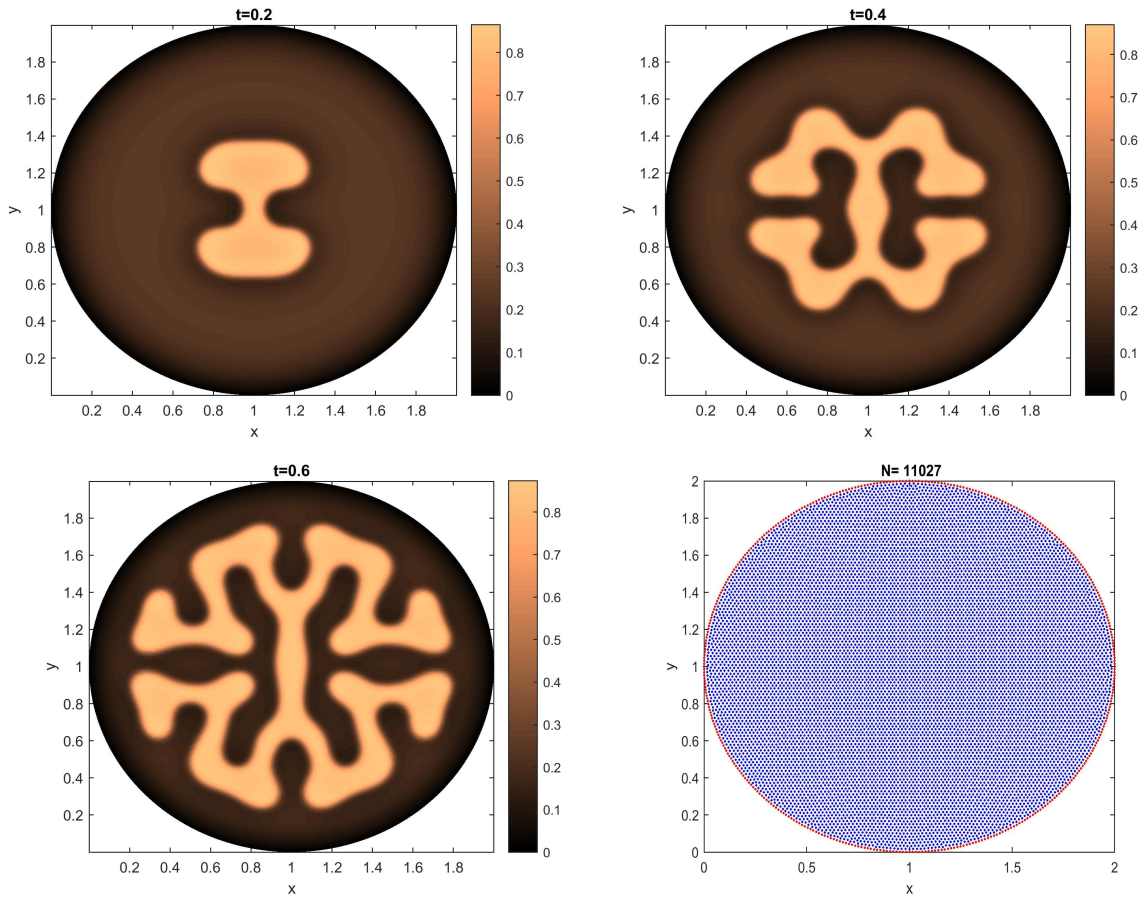


Figure 10: The numerical solution of tumor phase field φ at different time levels using $N = 11027$ uniform nodes restricted to the unit disk centered in $(1, 1)$.

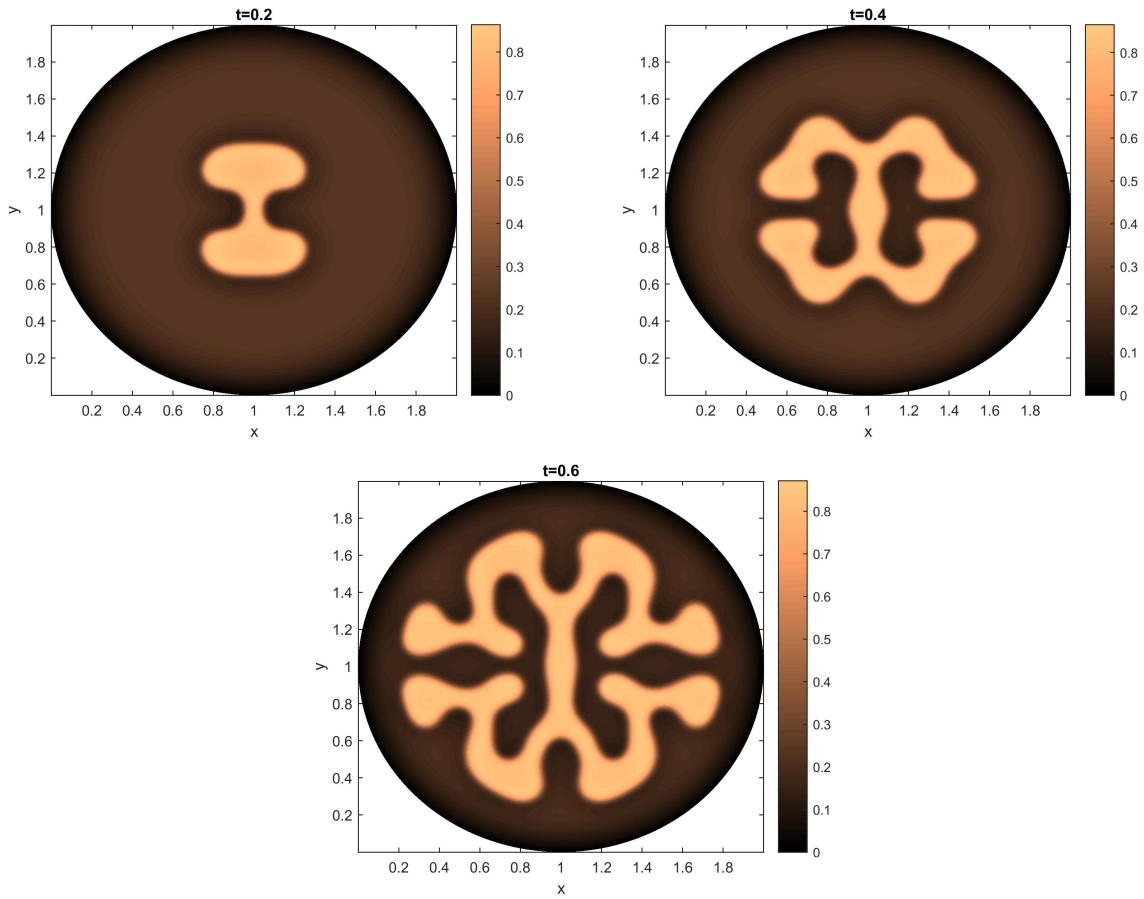


Figure 11: The numerical solution of tumor phase field φ at different time levels using $N = 22999$ uniform nodes.

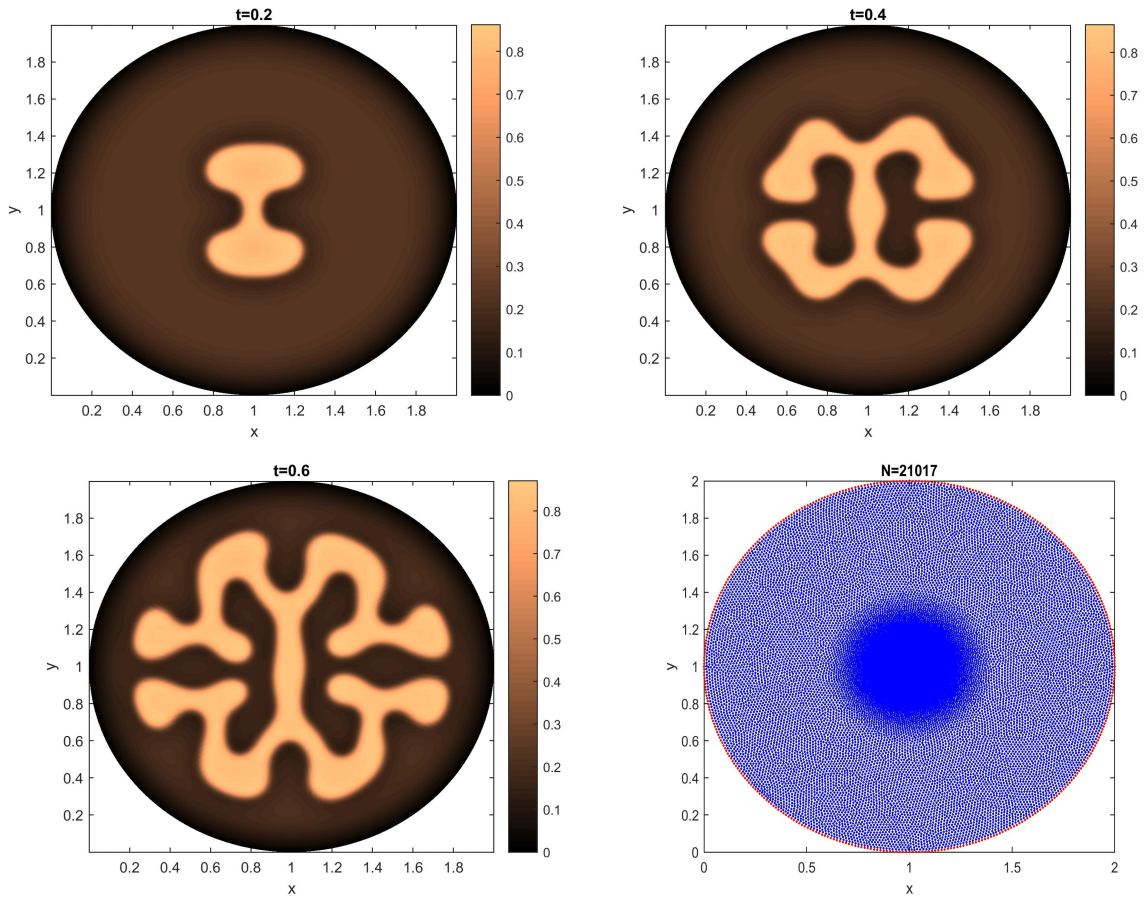


Figure 12: The numerical solution of tumor phase field φ at different time levels using $N = 21077$ quasi-uniform nodes with a different central density.

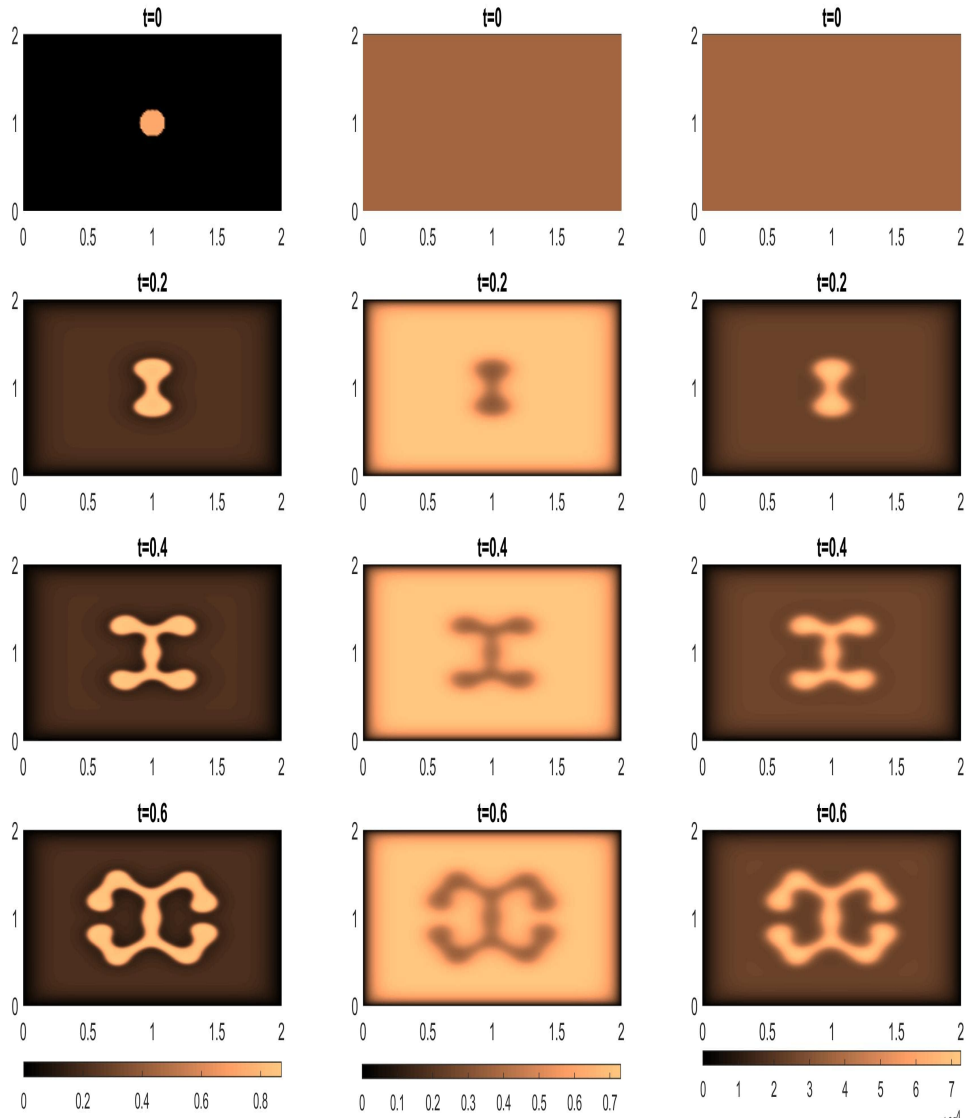


Figure 13: The numerical solution of tumor phase field φ , nutrient $\tilde{\sigma}$ and PSA \tilde{p} at different time levels using $N = 25921$ uniform nodes and $s = 2.60 \text{ g}/(L \cdot \text{day})$.

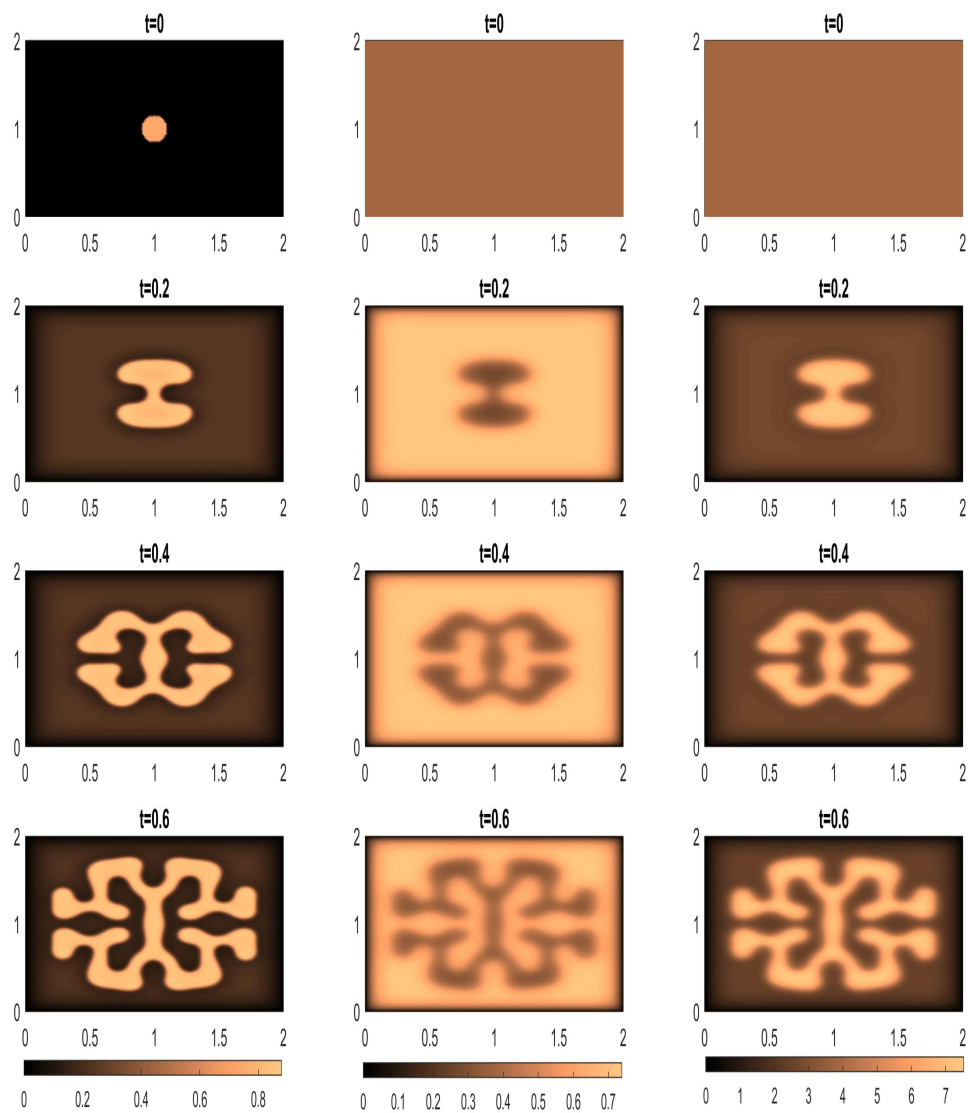


Figure 14: The numerical solution of tumor phase field φ , nutrient $\tilde{\sigma}$ and PSA \tilde{p} at different time levels using $N = 25921$ uniform nodes and $s = 2.70 \text{ g}/(L \cdot \text{day})$.

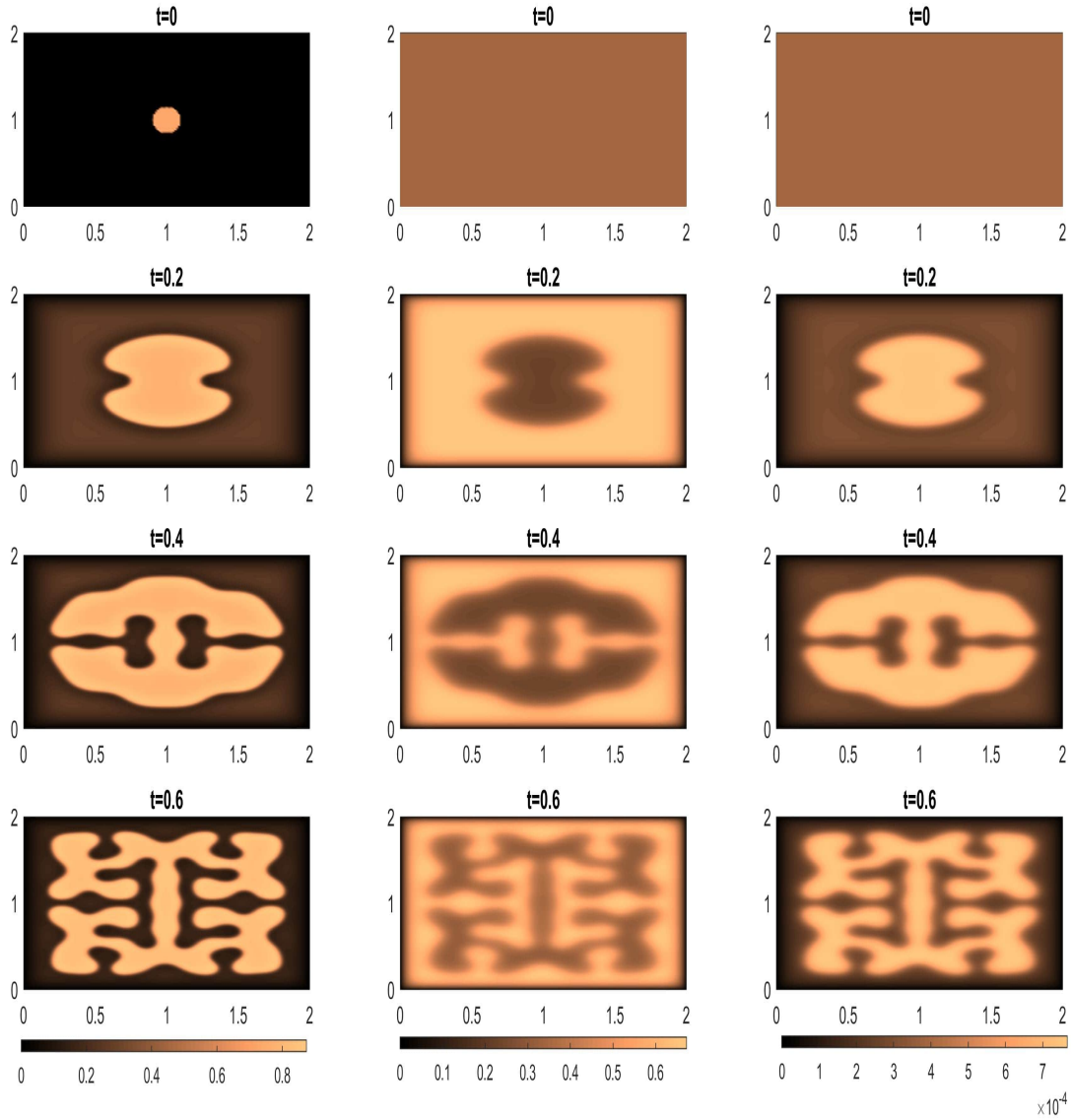


Figure 15: The numerical solution of tumor phase field φ , nutrient $\tilde{\sigma}$ and PSA \tilde{p} at different time levels using $N = 25921$ uniform nodes and $s = 2.80 \text{ g}/(L \cdot \text{day})$.

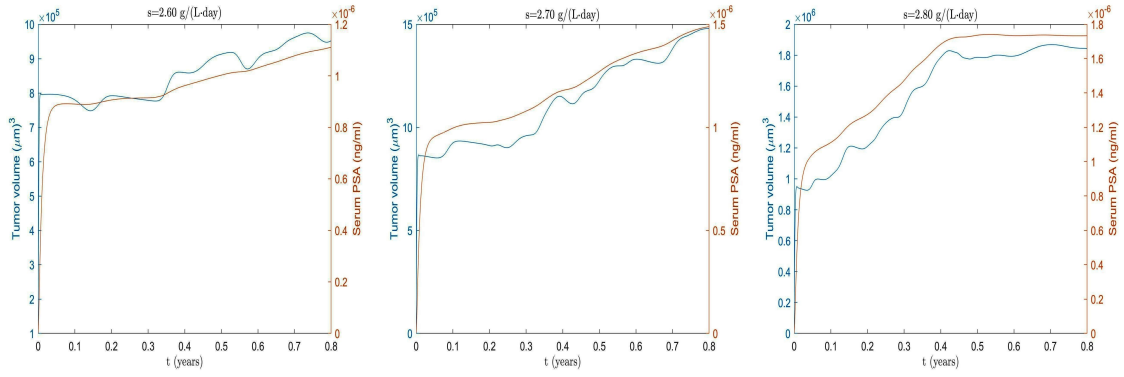


Figure 16: Tumor volume and serum PSA for different values of s at different time levels.

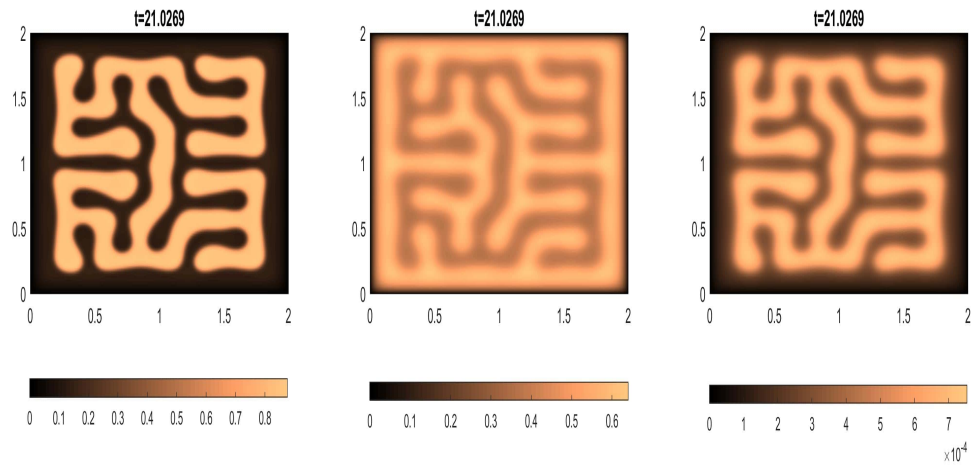


Figure 17: The steady-state solutions of φ , $\tilde{\sigma}$ and \tilde{p} via $N = 25921$ uniform points.

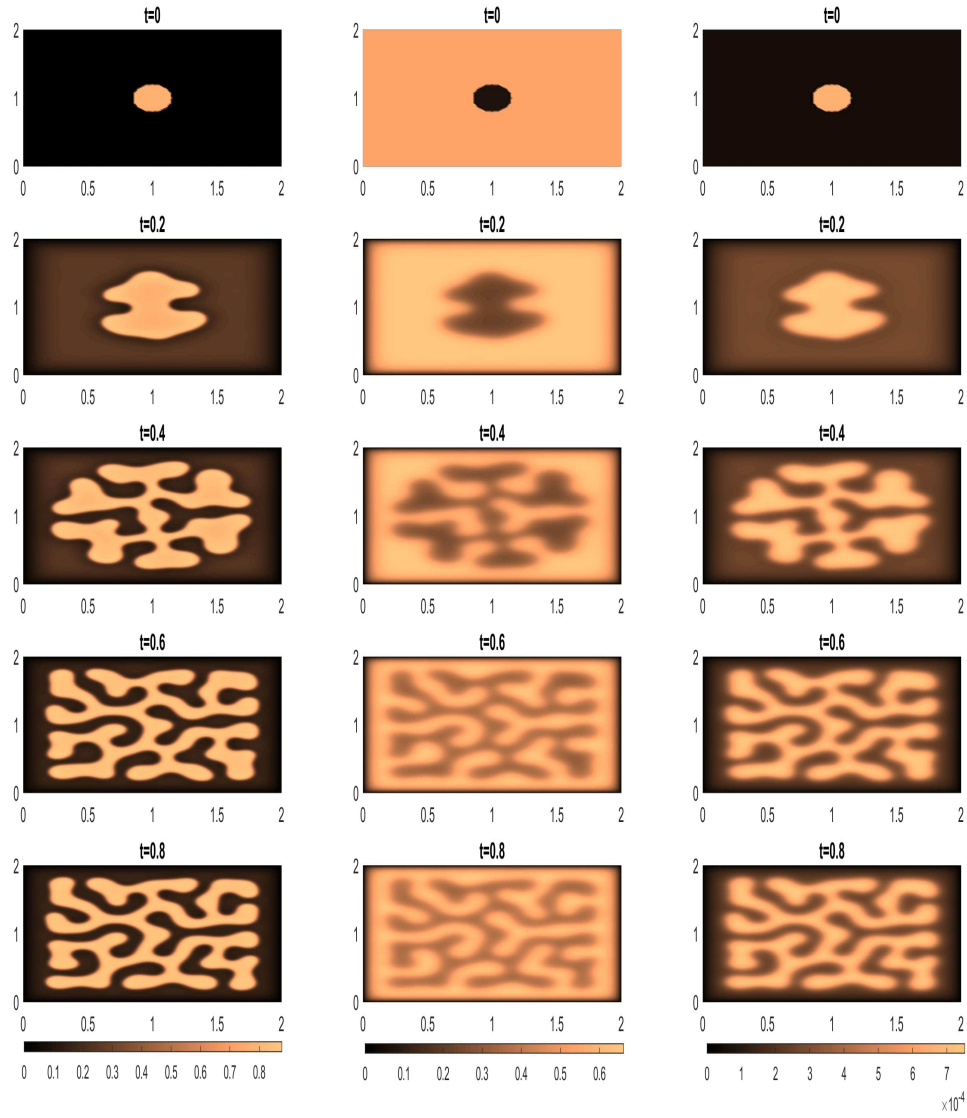


Figure 18: The numerical solution of tumor phase field φ , nutrient $\tilde{\sigma}$ and PSA \tilde{p} at different time levels using $N = 25921$ uniform nodes for $s = (2.75 + c) g/(L \cdot \text{day})$ with a mild heterogeneity c .

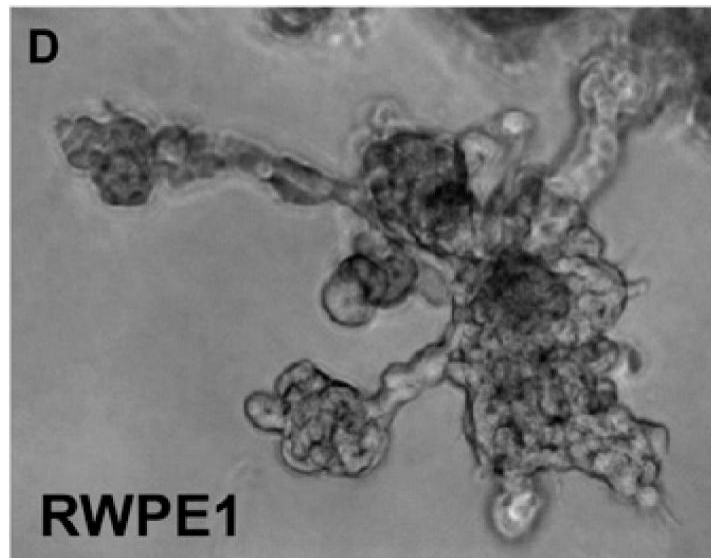


Figure 19: The fingered tumor growth patterns as observed in clinical practice and experiments ($\lambda = 5 \times 10^{-11} \text{ cm}^2/s$ and $\epsilon = 2 \times 10^{-9} \text{ cm}^2/s$). This picture is taken from [50], which authors of [50] had borrowed from [41].